MNRAS **542**, 3206–3230 (2025) Advance Access publication 2025 September 1



Downloaded from https://academic.oup.com/mnras/article/542/4/3206/8245131 by :: user on 21 October 2025

The case for large-scale AGN feedback in galaxy formation simulations: insights from XFABLE

Leah Bigwood,^{1,2}★ Martin A. Bourne ¹⁰, ^{1,2,3} Vid Iršič, ^{2,4,5,6,7} Alexandra Amon ¹⁰8,2 and Debora Sijacki^{1,2}

Accepted 2025 August 26. Received 2025 August 20; in original form 2025 January 30

ABSTRACT

While cosmological simulations of galaxy formation have reached maturity and are able to reproduce many fundamental galaxy and halo properties, no consensus has yet been reached on the impact of 'baryonic feedback' on the non-linear matter power spectrum. This severely limits the precision of (and potentially biases) small-scale cosmological constraints obtained from weak lensing and galaxy surveys. Recent observational evidence indicates that 'baryonic feedback' may be more extreme than commonly assumed in current cosmological hydrodynamical simulations. In this paper, we therefore explore a range of empirical active galactic nucleus (AGN) feedback models, within the FABLE simulation suite, with different parametrizations as a function of cosmic time, host halo properties, and/or spatial location where feedback energy is thermalized. We demonstrate that an AGN radio-mode feedback acting in a larger population of black holes, with jets thermalizing at relatively large cluster-centric distances, as exemplified by our XFABLE model, is in good agreement with the latest weak lensing + kSZ constraints across all k-scales. Furthermore, XFABLE maintains good agreement with the galaxy stellar mass function, and gas fraction measurements, as well as consistency with key galaxy group and cluster properties, including scaling relations and intracluster medium radial profiles, within current observational uncertainties. Our work highlights the pressing need to model black hole accretion and feedback physics with a greater level of realism, including relativistic magnetized jets in full cosmological simulations. Finally, we discuss how a range of complementary observational probes in the near future will enable us to constrain AGN feedback models, and therefore reduce 'baryonic feedback' modelling uncertainty for the upcoming era of large cosmological surveys.

Key words: black hole physics – methods: numerical – galaxies: formation – large-scale structure of Universe.

1 INTRODUCTION

The Lambda cold dark matter (ΛCDM) model of cosmology has proven extremely successful when stress-tested against observations over a remarkable span of cosmic history, from low-redshift measurements of the expansion history probed by baryonic acoustic oscillations (e.g. DESI Collaboration 2025a) and growth of structure (e.g. DESI Collaboration 2025b) to the accurate measurements of anisotropies and lensing of the cosmic microwave background (CMB; Planck Collaboration VI 2020; Pan et al. 2023; Madhavacheril et al. 2024). The ΛCDM model assumes the Universe comprises three main components: dark energy in the form of a cosmological constant (Λ), which drives an accelerated expansion of the Universe, CDM, which interacts only gravitationally, and the ordinary baryonic matter, which is, in principle, observable.

However, it is challenging to map baryons on to the underlying dark matter distribution due to the complex physical processes that regulate baryons' properties, such as gas radiative cooling and heating, star formation and associated stellar feedback, and black hole accretion and feedback physics, which are often referred to by the umbrella term 'baryonic feedback' (Semboloni et al. 2011; van Daalen et al. 2011; Vogelsberger et al. 2020). These processes influence the total matter distribution through the gas heating and cooling, the ejection and redistribution of gas (within and) beyond the virial radii of groups and clusters, and the back-reaction on the CDM distribution. Therefore, tests of the ACDM model on relatively small non-linear scales, such as through measurements of weak galaxy lensing, require accurate models of how 'baryonic feedback' impacts the overall matter distribution (Chisari et al. 2019; Schneider et al. 2019; Amon & Efstathiou 2022; Preston, Amon & Efstathiou 2023).

Hydrodynamical simulations have implemented active galactic nucleus (AGN) feedback models to demonstrate that it is necessary

¹Institute of Astronomy, University of Cambridge, Madingley Road, Cambridge CB3 0HA, UK

² Kavli Institute for Cosmology (KICC), University of Cambridge, Madingley Road, Cambridge CB3 0HA, UK

³Department of Physics, Centre for Astrophysics Research, Astronomy and Mathematics, University of Hertfordshire, College Lane, Hatfield AL10 9AB, UK

⁴SISSA – International School for Advanced Studies, Via Bonomea 265, I-34136 Trieste, Italy

⁵IFPU, Institute for Fundamental Physics of the Universe, Via Beirut 2, I-34151 Trieste, Italy

⁶INFN, Sezione di Trieste, Via Valerio 2, I-34127 Trieste, Italy

⁷INAF – Osservatorio Astronomico di Trieste, Via G. B. Tiepolo 11, I-34143 Trieste, Italy

⁸Department of Astrophysical Sciences, Princeton University, Peyton Hall, Princeton, NJ 08544, USA

^{*} E-mail: lmb224@cam.ac.uk

to regulate the star formation rate in massive galaxies and prevent overcooling of gas in groups and clusters (see Sijacki et al. 2007, McCarthy et al. 2010, Fabjan et al. 2010 for early studies, and a recent review by Bourne & Yang 2023). The impact of AGN feedback on the matter distribution is to suppress the matter power spectrum by up to ~ 30 per cent on the non-linear scales with respect to a darkmatter-only scenario; however, the simulations significantly differ in their predictions for the amplitude and scale dependence of the suppression at scales $0.1 h \text{ Mpc}^{-1} < k < 10 h \text{ Mpc}^{-1}$ (McCarthy et al. 2017; Springel et al. 2018; Chisari et al. 2019; van Daalen, McCarthy & Schaye 2020; Pakmor et al. 2023; Schaye et al. 2023; Gebhardt et al. 2024; Martin-Alvarez et al. 2024; Schaller et al. 2025). These inconsistent predictions can be attributed to a number of factors. The modelling choices of the astrophysical feedback processes can have a large outcome on the predicted matter power spectrum suppression (Daalen et al. 2011, 2020; Pandey et al. 2023), in addition to the adopted box size, resolution and hydrodynamical scheme by different studies. Despite the differences in feedback modelling (and the resulting matter power spectrum suppression), the state-of-the-art hydrodynamical simulations give reasonably similar matches to other observations, such as the galaxy stellar mass function (GSMF) and X-ray observations of cluster gas mass fractions, albeit noting a significant range of observed gas fractions at a given halo mass.

The current level of uncertainty in feedback modelling stands as the limiting factor for the precision of cosmological constraints from weak galaxy lensing (Amon et al. 2022; Dark Energy Survey and Kilo-Degree Survey Collaboration 2023). Beyond that, 'baryonic feedback' may have a role in the so-called 'S₈ tension' associated with the ΛCDM model. Over the last decade, discrepancies in the measurements of the clustering amplitude parameter,¹ $S_8 = \sigma_8(\Omega_{\rm m}/0.3)^{0.5}$, by weak galaxy lensing surveys with respect to Planck ACDM best-fitting cosmology have persisted. Amon & Efstathiou (2022) and Preston et al. (2023) hypothesized that 'baryonic feedback' could be responsible if it had a stronger impact on the nonlinear matter distribution than that predicted by many state-of-the-art hydrodynamical simulations. Indeed, the proposal for more extreme feedback has been supported by recent evidence from cosmic shear and stacked kinetic Sunyaev-Zeldovich measurements (kSZ; Bigwood et al. 2024), measurements of the kSZ effect (Hadzhivska et al. 2024; McCarthy et al. 2024), cross-correlations of weak lensing with diffuse X-ray and thermal SZ (tSZ; Ferreira et al. 2024; La Posta et al. 2025), and measurements of the tSZ effect, including the power spectrum (Ruan, McQuinn & Anderson 2015; Crichton et al. 2016; Dutta Chowdhury & Chatterjee 2017, Efstathiou & McCarthy 2025). However, it remains a challenge to identify a physical mechanism to produce stronger feedback that remains in accord with galaxy group and cluster X-ray data, not only in terms of gas fractions but also of spatially resolved intracluster medium (ICM) properties.

Feedback effects are among a number of 'sub-grid' processes that occur below the resolution scale of cosmological simulations and are therefore modelled through empirical prescriptions that aim to capture the complex small-scale physics. In a widely adopted but simplistic picture, AGN feedback is often modelled using two primary modes, dependent on the accretion rate of the supermassive black hole (SMBH), or more specifically the Eddington ratio (Sijacki

et al. 2007). The quasar-mode (or 'thermal-mode') acts at high SMBH accretion rates and is often attributed to high-velocity quasardriven winds directly impacting the host galaxy and circumgalactic medium (CGM) (Mullaney et al. 2013; Harrison et al. 2014). The radio-mode (or 'kinetic-mode') is instead associated with inefficient SMBH accretion and launches AGN jets impacting the CGM and the ICM. These jets inflate expanding bubbles, displacing the hot gas and leaving cavities and shock-fronts detectable in X-ray images of galaxy groups and clusters (Fabian 2012). Some hydrodynamical simulations distinguish between the two modes by imposing both thermal and kinetic outflows, with others opting for a purely thermal feedback model, regardless of the SMBH accretion state. It should be noted however that observationally this picture is less clear, both in terms of the roles that different forms of feedback (i.e. radiation, winds, and jets) play in galaxy evolution and under what conditions they are produced, with radio jets being observed in systems undergoing accretion at high, as well as low Eddington ratios (see e.g. Hardcastle & Croston 2020; Hlavacek-Larrondo, Li & Churazov 2022, for reviews).

The choice of sub-grid parameters utilized to model feedback processes in simulations also plays a role in the varying predictions of the matter power spectrum suppression. Although physical arguments can be used to narrow the range of plausible parameter values of the feedback models, they are typically poorly constrained and often resolution-dependent. As such, calibrating to external observational data sets is required. Observations of the GSMF, star formation history, and stellar sizes are all frequently used to guide hydrodynamical simulations. However, the hot gas mass fractions of groups and clusters, measured using X-ray observations, are generally the key benchmark of the AGN feedback model efficacy (e.g. McCarthy et al. 2017; Henden et al. 2018; Schaye et al. 2023).

In this paper, we explore the potential for more extreme AGN feedback in hydrodynamical simulations. Using the FABLE simulation framework (Henden et al. 2018; Henden, Puchwein & Sijacki 2019, 2020) as a test-bed, we explore an extensive number of modifications to the AGN feedback model in FABLE, to demonstrate that it is possible to produce the more extreme matter power spectrum suppression required to resolve the S₈ tension and remain consistent with new observational weak lensing, tSZ, and kSZ constraints while still maintaining consistency with key galaxy and cluster observables typically used to calibrate simulations, as exemplified by our new empirical AGN feedback model, XFABLE. We stress that it is crucial that the potential degeneracies within hydrodynamical simulations are understood if weak lensing analyses are to continue utilizing them to calibrate their 'baryonic feedback' mitigation.

The paper is structured as follows. In Section 2 we motivate the study by discussing the spread in the suppression of the matter power spectrum predicted by a range of hydrodynamical simulations, despite each providing a good fit to GSMF and cluster gas mass fractions observations. Section 3 describes the basic properties of the simulation suite we utilize. It also details the computation of a number of galaxy, group, and cluster properties from the simulation outputs to allow for comparison to observations. Section 4 describes the key modifications to the FABLE AGN feedback model we test in this work, including XFABLE, and the motivations behind the models. In Section 5 we compare the predictions made by each of our key simulation boxes to a range of observational measurements. Finally, in Section 6 we summarize our findings from the simulation suite and discuss the outlook for XFABLE.

¹Here, $\Omega_{\rm m}$ is the ratio of the present-day matter density to the critical density of the Universe and σ_8 is the root mean square linear amplitude of the matter fluctuation spectrum in spheres of radius 8 h^{-1} Mpc extrapolated to the present day.

2 THE UNCERTAINTY IN SIMULATING BARYONIC FEEDBACK AND IMPLICATIONS FOR S₈ TENSION

Hydrodynamical simulations are increasingly sophisticated in their ability to reproduce realistic cosmic populations of galaxies, galaxy groups, and clusters. Nevertheless, there is a lack of agreement in the predictions from the state-of-the-art simulations, with one particularly salient example being the impact of baryonic physics on the matter power spectrum (Chisari et al. 2019; Daalen et al. 2020). Weak lensing analyses (in addition to i.e. N×2pt analyses involving tSZ and kSZ data and effective field theory analyses of galaxy clustering) require an accurate prediction of the suppression of the matter power spectrum due to feedback to infer cosmological parameters, especially if they are to use the (mildly) non-linear scales. Marginalizing over this spread of possible predictions already dominates the systematic uncertainty (e.g. Bigwood et al. 2024). To maximize the statistical power of the surveys, a coherent and consistent picture of feedback's impact on the total matter distribution is critical

In this section, to demonstrate this problem, we discuss the z=0 predictions of the matter power spectrum suppression, GSMF, and hot gas fraction in groups and clusters from a number of state-of-the-art cosmological hydrodynamical simulations and compare them with available observations. We show the latter two observables as these are typically the key properties used to calibrate the feedback parameters in simulations. Indeed, simulations have shown a remarkable ability to reproduce a wide range of other observables when (largely) calibrated to these two key measurements (McCarthy et al. 2017; Henden et al. 2018; Schaye et al. 2023).

Fig. 1 shows these properties as measured in the fiducial FABLE (40 $h^{-1}{\rm Mpc})^3$ box (hereinafter FABLE-40) (Henden et al. 2018), as well as a larger (100 $h^{-1}{\rm Mpc})^3$ box we run, employing the fiducial FABLE physics model (hereinafter FABLE-100).² We refer the reader to Section 3 for an introduction to the FABLE simulation properties. We compare to FLAMINGO L1_m9 [Schaye et al. 2023; Schaller et al. 2025, (1 Gpc)³ box with gas mass resolution of 10⁹ ${\rm M}_{\odot}$], MillenniumTNG [Pakmor et al. 2023, (740 Mpc)³ box with gas mass resolution of $3.1 \times 10^7 {\rm M}_{\odot}$], SIMBA [Davé et al. 2019, (100 $h^{-1}{\rm Mpc})^3$ box with gas mass resolution of $1.82 \times 10^7 {\rm M}_{\odot}$], and BAHAMAS [McCarthy et al. 2017, (400 $h^{-1}{\rm Mpc})^3$ box with AGN feedback parameter $\Theta_{\rm AGN} = 7.8$ and gas mass resolution of $7.66 \times 10^8 {\rm M}_{\odot}/h$].

2.1 Comparison of cosmological hydrodynamical simulations: the matter power spectrum suppression

The left panel of Fig. 1 shows the predicted suppression of the matter power spectrum from each simulation at z=0. We compare to the predicted suppression required to reconcile the DES Y3 cosmic shear S_8 constraint with the *Planck* Λ CDM model, $A_{\text{mod}}=0.858\pm0.052$ (Preston et al. 2023) (blue band).³ We also compare to the observa-

tional constraint from the joint weak lensing and kSZ (WL + kSZ) analysis presented in Bigwood et al. (2024) (purple band).

All of the hydrodynamical simulations predict suppression of the matter power spectrum on scales $k \ge 0.5 h \,\mathrm{Mpc^{-1}}$. However, there is no consensus on the amplitude or extent of suppression: at $k \sim$ 1 h Mpc⁻¹ the suppression predicted by the simulations displayed spans 1–5 per cent, and at $k \sim 5 h \, \mathrm{Mpc^{-1}}$ the range increases to 5–20 per cent. FLAMINGO, FABLE (see also a recent study by Martin-Alvarez et al. 2024), and MTNG740 predict a mild suppression, which is not consistent with the A_{mod} or WL + kSZ constraint, suggesting that if these simulations capture a realistic feedback scenario, baryonic effects are unable to resolve the S_8 tension. The simulations are not consistent with the larger scale suppression constrained by the data at $k \lesssim 2 h \, \text{Mpc}^{-1}$, except for SIMBA. To avoid overcrowding Fig. 1 we do not plot the Magneticum (Steinborn et al. 2015) or Horizon-AGN (Dubois et al. 2014) simulations, but we note Magneticum predicts a matter power spectrum suppression closely following BAHAMAS, and Horizon-AGN predicts a suppression close to that measured in MTNG740.

We note that the FABLE predictions for the two box sizes explored here are in good agreement with each other at $k < 3 h \, \text{Mpc}^{-1}$, and both show a maximum suppression at $k \sim 10 \, h \, \text{Mpc}^{-1}$. FABLE-100 shows a slightly larger peak suppression of \sim 13 per cent, compared to \sim 10 per cent in the FABLE-40 box. This result is consistent with the impact of box size found in Springel et al. (2018). We additionally found that there was no systematic difference between the two FABLE boxes when investigating the matter power spectrum suppression with redshift. We conclude that the greater peak suppression in the FABLE-100 box at z = 0 likely results from the stochastic nature of radio-mode feedback in massive haloes.

$\begin{tabular}{ll} \bf 2.2 & Comparison of cosmological hydrodynamical simulations: \\ the GSMF \end{tabular}$

The GSMF is sensitive to the baryonic processes governing star formation, including cooling, stellar, and AGN feedback channels. As it is tightly constrained by data at z=0, it provides a good test of galaxy formation models and has been used to calibrate the above simulations. In the middle panel of Fig. 1, we show the GSMF measurements of D'Souza et al. (2015), Baldry et al. (2012), Bernardi et al. (2013), Driver et al. (2022), and Li & White (2009). We compare these measurements with the FABLE simulations, as well as FLAMINGO, MTNG740, SIMBA, and BAHAMAS.

Generally, each simulation is in good agreement with the observations.⁴ We note that both FABLE boxes show similarly good agreement with observational data, with the larger FABLE-100 box being able to better sample rare high stellar mass galaxies $(\log_{10}(M_*[M_\odot]) \sim 12)$, and hence extend the GSMF tail.⁵ Nevertheless, it is notable that independent simulations, in similarly good agreement with GSMF observations (at least at z = 0) given

should ideally be done at $z\sim0.4$, but as simulation predictions are not readily available, we plot all simulation results at z=0. For the FABLE-only analysis that we present later (see Fig. 3), we discuss the redshift dependence.

⁴Note that MTNG740 predictions for galaxies with stellar mass $\log_{10}(M_*[\mathrm{M}_\odot]) < 11$ largely stem from the effective mass resolution of the simulations, with higher resolution TNG results in much closer agreement with the data (for further details see Pakmor et al. 2023).

⁵For massive galaxies, the GSMF is overpredicted by FABLE. Further refinements in baryonic 'sub-grid' physics, and a different choice of the stellar mass aperture (such as the commonly adopted 30 kpc fixed aperture), may improve the agreement, but this is beyond the scope of this paper.

 $^{^2}$ We note that in this work, we run all simulations, including FABLE-40, using a different random seed that determines the initial Gaussian density field to that utilized for the $(40\ h^{-1}{\rm Mpc})^3$ presented in Henden et al. (2018) and Martin-Alvarez et al. (2024). We therefore find a small difference in the measured matter power spectrum suppression, which lies within the span of the scatter in the suppression due to cosmic variance (see Appendix A).

³The DES Y3 lensing kernel, which defines the redshift sensitivity of the sample, peaks at $z \sim 0.4$ (Amon et al. 2022). Since the best-fitting A_{mod} constraint has no explicit redshift dependence, a comparison to simulations

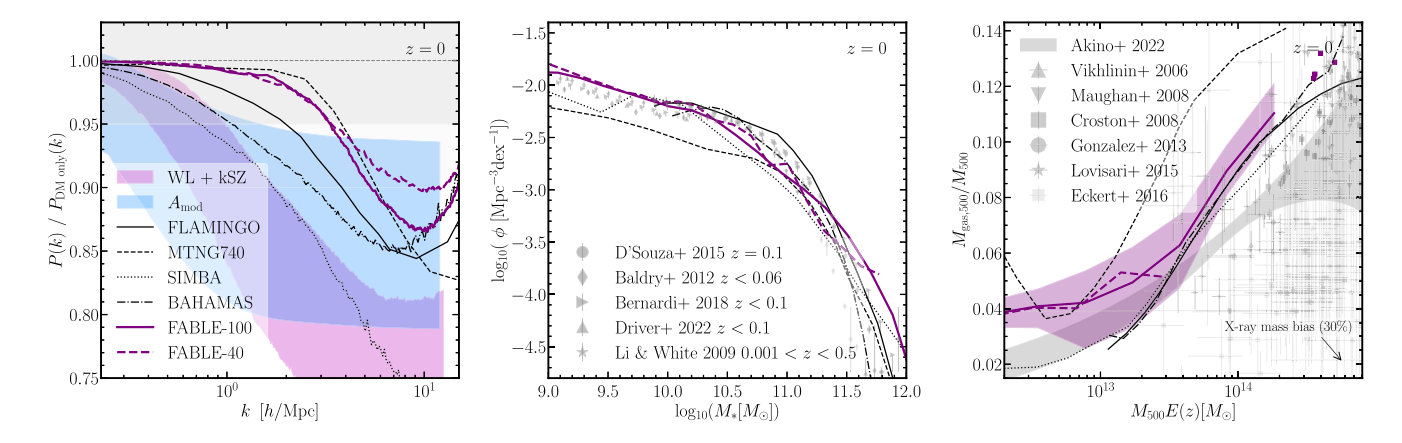


Figure 1. The z=0 properties of the FABLE-40 (dashed purple line) and FABLE-100 (solid purple line) simulations compared to observational constraints and other hydrodynamical simulations; FLAMINGO L1_m9 (hereafter denoted as FLAMINGO) (Schaye et al. 2023; Schaller et al. 2025, black solid line), MTNG740 (Pakmor et al. 2023, black dashed line), SIMBA (Davé et al. 2019, black dotted line), and BAHAMAS (McCarthy et al. 2017, black dash–dotted line). Left: the matter power spectrum suppression due to baryonic effects, $P(k)/P_{\rm DMonly}(k)$, compared to the $A_{\rm mod}=0.858\pm0.052$ constraint (blue, shaded; Preston et al. 2023), and the constraint from the combined DES Y3 cosmic shear and ACT kSZ (WL + kSZ) analysis of Bigwood et al. (2024) (purple, shaded). Centre: the GSMF for the above-mentioned simulation projects and FABLE. We further plot observational measurements of D'Souza, Vegetti & Kauffmann (2015) (z=0.1), Baldry et al. (2012) (z<0.06), Bernardi et al. (2018) (z<0.1), Driver et al. (2022) (z<0.1), and Li & White (2009) (0.001 < z<0.5) as the grey errorbars. Right: the hot gas fraction measured within r_{500} as a function of halo mass M_{500} or the above-mentioned simulation projects and FABLE. For FABLE-40 and FABLE-100, lines denote the median relation and the purple band denotes the quartiles of the distribution in FABLE-100. For FABLE-100, we plot the most massive systems that cannot be binned due to poor statistics as individual data points. The grey data points are the measurements of Vikhlinin et al. (2006) (z<0.25), Maughan et al. (2008) (0.1 < z<1.3), Croston et al. (2008) (z<0.2), Gonzalez et al. (2013) (z<0.2), Lovisari, Reiprich & Schellenberger (2015) (z<0.4), and Eckert et al. (2016) (0.05 < z<1.1), and the grey shaded regions show the 1σ constraints of Akino et al. (2022) (z<1). We demonstrate that despite each simulation showing reasonable fits to observations, the predictions for the suppression of the matter power spectrum at z=0 vary significantly.

the observed uncertainties, predict significantly different baryonic suppression of the matter power spectrum.

2.3 Comparison of cosmological hydrodynamical simulations: hot gas fractions in groups and clusters

The mass fractions of gas and stars in simulated groups and clusters are very sensitive to the AGN feedback modelling. Furthermore, the total baryon fraction has been shown to be directly related to the matter power spectrum suppression (Daalen et al. 2020; Salcido et al. 2023; Martin-Alvarez et al. 2024). The right panel of Fig. 1 shows the hot gas fraction in groups and clusters, where simulation predictions from FABLE, FLAMINGO, MTNG740, SIMBA, and BAHAMAS are plotted. For the FABLE-100 box, in addition to the median, we show the quartiles of the gas fraction distribution as the purple-shaded band.⁷ For comparison, we plot the X-rayderived measurements of Akino et al. (2022),8 Vikhlinin et al. (2006) (z < 0.25), Maughan et al. (2008) (0.1 < z < 1.3), Croston et al. (2008) (z < 0.2), Gonzalez et al. (2013) (z < 0.2), Lovisari et al. (2015) (z < 0.4), and Eckert et al. (2016) (0.05 < z < 1.1). We note that the cluster masses of Akino et al. (2022) and Eckert et al. (2016) are derived via weak lensing estimates, whereas the remaining sources use X-ray hydrostatic cluster masses. The latter are derived

under the assumption of hydrostatic equilibrium and hence may underestimate the true halo mass by 10–35 per cent (e.g. due to neglecting non-thermal pressure support), with the exact magnitude of the bias still debated (see Pratt et al. 2019, for a review). For illustrative purposes, the arrow indicates the effect on observations to correct for a 30 per cent mass bias.

The two FABLE boxes are in very good agreement for groups of mass $M_{500} < 10^{14} \rm \ M_{\odot}$, with the FABLE-100 box having a large enough sample of clusters to compute the gas fractions up to $M_{500} \sim 4 \times 10^{14} \rm \ M_{\odot}$. FABLE-100 displays a very good match to the data, as well as the predictions from FLAMINGO, BAHAMAS, and SIMBA. However, the scatter in the observed data is significant. We therefore re-emphasize the point made in the previous section: AGN feedback models that produce reasonable gas fractions (within the large observed scatter) exhibit a large discrepancy in the matter power spectrum suppression for cosmological studies.

We further observe that the gas fraction—halo mass relation measured in a hydrodynamical simulation could lie up to $\sim 3\sigma$ lower than the one measured in FABLE-100 while still remaining within the large scatter of the data. More powerful AGN feedback responsible for this greater expulsion of gas may, in theory, then produce a power spectrum suppression greater than that predicted by the simulations in the left panel of Fig. 1. Moreover, provided the observed scatter is real, it remains to be understood if simulations need to produce a larger variety of gas fractions at a given halo mass, which would point towards a more stochastic nature of AGN feedback and more extreme feedback for a sub-set of objects.

Motivated by these findings, we explore the possibility of AGN feedback that produces a more extreme matter power spectrum

⁶We note that the FLAMINGO suite has also explored more extreme feedback variants that exhibit gas mass fractions lower than the fiducial FLAMINGO L1_m9 box we compare to (see table 2 of Schaye et al. 2023 and Schaller et al. 2025).

⁷In Fig. 1, and throughout the remainder of the work, the shaded bands showing the quartile regions finish at the mid-point of the highest bin.

⁸We note that unlike the remainder of the observational data sets where we plot individual objects, we plot the best-fitting relation of Akino et al. (2022), as the data are model-dependent on error correlation considerations.

⁹We note again the exception of MTNG740, which is at the upper end of the observations and the other simulations displayed, and refer the reader to Pakmor et al. (2023) where this result was initially discussed.

suppression, in better agreement with observational constraints, while preserving the match to the observed gas fractions and GSMF.

3 METHODOLOGY

3.1 Numerical code and basic simulation properties

In this study, simulations are performed with the massively parallel moving-mesh code AREPO (Springel 2010; Pakmor et al. 2016). The TreePM approach is used for computing gravitational interactions and hydrodynamics is solved on a quasi-Lagrangian Voronoi mesh, which approximately moves with the local flow velocity.

As a starting point, we adopt the FABLE simulation model. Its key characteristics are described below and we refer the reader to Henden et al. (2018, 2019, 2020) for a more detailed discussion. In a nutshell, the FABLE project adopts the same sub-grid models for gas radiative cooling (Katz, Weinberg & Hernquist 1996; Wiersma, Schaye & Smith 2009a), chemical enrichment (Wiersma et al. 2009b), and star formation (Springel & Hernquist 2003), subject to a spatially uniform UV background (Katz et al. 1996; Faucher-Giguère et al. 2009), as developed for the Illustris project (Vogelsberger et al. 2013; Torrey et al. 2014). While the Illustris simulation models stellar winds in a purely kinetic fashion at launch, in FABLE, one-third of the wind energy is thermal (Marinacci, Pakmor & Springel 2014; Henden et al. 2018). The fiducial FABLE model adopts two modes for AGN feedback: a quasar-mode for black holes in the radiatively efficient accretion regime (Di Matteo, Springel & Hernquist 2005; Springel, Di Matteo & Hernquist 2005) and a radio-mode feedback for the radiatively inefficient accretion regime (Sijacki et al. 2007), as in the Illustris model (Sijacki et al. 2015). The quasar-mode thermally and isotropically couples a fraction of the available feedback energy to the surrounding gas, whereas the radio-mode injects hot bubbles at some distance from the black hole, mimicking the radio lobes inflated by 'mechanical' feedback. Compared to Illustris, the two main differences in FABLE stem from adopting a fixed duty cycle in the quasar-mode, instead of injecting thermal energy continuously (see Booth & Schaye 2009; Henden et al. 2018), and from reducing the duty cycle of radio bubble inflation, which leads to a more frequent but less energetic radio-mode feedback. We note that stellar and AGN feedback in FABLE have been calibrated to reproduce the GSMF and the gas mass fractions of massive haloes in the local Universe (see also McCarthy et al. 2017; Schaye et al. 2023, for a similar calibration strategy). We perform uniform cosmological boxes and do not consider the zoom-in group and cluster simulations from the original FABLE suite.

We build a suite of $40 h^{-1}$ cMpc-side simulation boxes to explore the effect of AGN feedback modifications to the FABLE model and cosmic variance (see Appendix A). These boxes have 512³ dark matter particles and gas cells (approximately), corresponding to a dark matter particle mass $m_{\rm DM} = 3.4 \times 10^7 \, h^{-1} \rm M_{\odot}$ and mean target gas cell mass $\bar{m}_{\rm gas} = 6.4 \times 10^6 \, h^{-1} \rm M_{\odot}$. We set the gravitational softening length to $2.4 h^{-1}$ pkpc (physical coordinates) below z = 5and fix it in comoving coordinates at higher redshifts by following the empirical recommendation of Power et al. (2003). To ensure we have a sufficient statistical sample of galaxy groups and (low mass) galaxy clusters, we run two further cosmological boxes with a side length of $100 h^{-1}$ cMpc, both for the fiducial FABLE baryonic physics model (FABLE-100) and for one of our new modified AGN feedback models, which henceforth we denote as 'XFABLE-100'. These larger boxes have the same mass and spatial resolution as the $40 h^{-1}$ cMpc on-a-side boxes, tracking 1280^3 dark matter particles and $\sim 1280^3$ gas cells. Boxes are evolved to z = 0 and adopt initial conditions consistent with the cosmological parameters measured by Planck Collaboration VI (2020) ($\Omega_{\Lambda}=0.6856$, $\Omega_{\rm M}=0.3144$, $\Omega_{\rm b}=0.0494$, $\sigma_8=0.8154$, $n_s=0.9681$, and $H_0=67.32$ km s⁻¹ Mpc⁻¹).

3.2 Black hole accretion and feedback in FABLE-like simulation models

In this work we focus on modifications to the AGN feedback model, since it has been shown to have the dominant effect in causing suppression of the matter power spectrum (see e.g. Chisari et al. 2019; Daalen et al. 2020; Martin-Alvarez et al. 2024). We first describe the fiducial FABLE black hole accretion and feedback model. Summaries of the key model parameters and their values in both the fiducial FABLE and the XFABLE models are listed in Table 1.

Black hole formation proceeds by placing seed black holes of mass $10^5~h^{-1}~M_{\odot}$ into every halo of mass greater than $5\times10^{10}~h^{-1}~M_{\odot}$, where haloes are identified using a fast friend-of-friend (FoF) algorithm on the fly. Black holes are modelled as collisionless sink particles and are able to grow in mass through black hole mergers and gas accretion.

The black hole accretion rate, $\dot{M}_{\rm BH}$, is given by the Bondi–Hoyle–Lyttleton formula, where a dimensionless parameter, α , boosts the accretion rate as

$$\dot{M}_{\rm BH} = \frac{4\pi\alpha G^2 M_{\rm BH}^2 \rho}{c_s^3} \,, \tag{1}$$

where ρ and c_s are the gas density and sound speed, respectively. Note that $\dot{M}_{\rm BH}$ is capped at the Eddington limit. In the radiatively efficient regime, the black hole bolometric luminosity, $L_{\rm bol}$, is given by

$$L_{\text{bol}} = \epsilon_r \dot{M}_{\text{BH}} c^2 \,, \tag{2}$$

where ϵ_r is the radiative efficiency and c is the speed of light.

Feedback occurs in one of two modes, solely determined by the ratio of the accretion rate of the black hole to the Eddington rate, $f_{\rm BH} = \dot{M}_{\rm BH}/\dot{M}_{\rm Edd}$. If the black hole is accreting efficiently and $f_{\rm BH}$ exceeds the threshold of $\chi_{\rm radio}$, the quasar-mode is operating. This is typically the dominant feedback process at high redshifts, where a copious gas supply maintains high black hole accretion rates. A fraction of the bolometric luminosity is coupled thermally and isotropically to the gas surrounding the black hole, ϵ_f , resulting in the feedback energy, $E_{\rm feed}$, being given by

$$\dot{E}_{\text{feed}} = \epsilon_f L_{\text{bol}} \,. \tag{3}$$

If the thermal energy injected into gas cells is unable to significantly raise the gas temperature (for example as the result of spreading the energy over a large gas mass), or is predominantly injected into high-density gas, then the energy can be radiated away before impacting the environment (Katz et al. 1996; Booth & Schaye 2009; Bourne, Zubovas & Nayakshin 2015). To prevent this numerical 'overcooling', the feedback energy is stored for the time period of the duty cycle, Δt , and the energy accumulated in this time period is released in a single feedback event (following a similar approach to Le Brun et al. 2014; Schaye et al. 2015).

For $f_{\rm BH} < \chi_{\rm radio}$, the radiatively inefficient radio-mode operates. Hot bubbles of radius, $R_{\rm bub}$, are injected at a random spatial position within a sphere of radius, $D_{\rm bub}$, from the black hole, to mimic injection by an unresolved AGN jet. This results in a largely isotropic feedback once averaged over sufficient time. The bubbles are periodically injected after the gain in the black hole's mass has

Table 1. The key parameters associated with black hole accretion and feedback in the FABLE and XFABLE models.

Parameter	Description	Value in FABLE	Value in XFABLE	
α	Dimensionless parameter boosting the black hole accretion rate (equation 1).	100		
Xradio	Accretion rate threshold in Eddington units separating quasar and radio-mode activity. The quasar-mode acts when $\dot{M}_{\rm BH}/\dot{M}_{\rm Edd} > \chi_{\rm radio}$, and the radio-mode when $\dot{M}_{\rm BH}/\dot{M}_{\rm Edd} < \chi_{\rm radio}$.	0.01	0.1	
ϵ_r	Radiative efficiency, determining the fraction of energy gained from mass accretion that may be converted to radiation (equation 2).	0.1	0.1	
ϵ_f	Thermal coupling associated with the quasar-mode, determining the fraction of	0.1	0.1	
	the bolometric luminosity to be converted to thermal energy (equation 3).			
Δt [Myr]	Duty cycle of the quasar-mode: the time for which feedback energy is stored before it is released in a single feedback event.	25	25	
$\epsilon_{ m m}$	Efficiency of mechanical heating associated with the radio-mode (equation 4).	0.8	0.8	
$\delta_{ m BH}$	Duty cycle of radio-mode; bubbles are injected after the mass gain of the black hole has exceeded $\delta_{\rm BH} = \delta M_{\rm BH}/M_{\rm BH}$.	0.01	0.01	
$D_{\text{bub}} [h^{-1}\text{kpc}]$	Distance bubbles are injected from the black hole in the radio-mode.	equation (5), with $D_{\text{bub},0} = 30$	100	
$R_{\rm bub} [h^{-1}{\rm kpc}]$	Radius of the injected bubbles in the radio-mode.	equation (6), with $R_{\text{bub},0} = 50$	50	

exceeded $\delta_{\rm BH} = \delta M_{\rm BH}/M_{\rm BH}$. The energy content of the resulting bubble is given by

$$E_{\text{bub}} = \epsilon_{\text{m}} \epsilon_{r} \delta M_{\text{BH}} c^{2} \,, \tag{4}$$

where $\epsilon_{\rm m}$ is the efficiency of this 'mechanical' heating. In the fiducial model, the bubble distance and radius are scaled with energy and ICM density, $\rho_{\rm ICM}$, according to

$$D_{\text{bub}} = D_{\text{bub},0} \left(\frac{E_{\text{bub}}/E_{\text{bub},0}}{\rho_{\text{ICM}}/\rho_{\text{ICM},0}} \right)^{1/5} , \qquad (5)$$

$$R_{\text{bub}} = R_{\text{bub},0} \left(\frac{E_{\text{bub}}/E_{\text{bub},0}}{\rho_{\text{ICM}}/\rho_{\text{ICM},0}} \right)^{1/5} , \qquad (6)$$

$$R_{\text{bub}} = R_{\text{bub},0} \left(\frac{E_{\text{bub}}/E_{\text{bub},0}}{\rho_{\text{ICM}}/\rho_{\text{ICM},0}} \right)^{1/5} , \tag{6}$$

where $D_{\text{bub},0}$, $R_{\text{bub},0}$, $E_{\text{bub},0}$, and $\rho_{\text{ICM},0}$ are normalization constants. This follows the studies Scheuer (1974), Begelman & Cioffi (1989), and Heinz, Reynolds & Begelman (1998), which show that more energetic AGN jets will lead to larger lobes at a greater distance from the black hole, and a greater ICM density will have the inverse effect of confining the bubbles.

Note that when we modify the FABLE AGN feedback model, we test removing the scaling of equation (5) and equation (6) and fixing R_{bub} and D_{bub} to specific values. In this scenario, the bubbles are injected at a random spatial position on a spherical shell (rather than within the sphere) of radius D_{bub} .

3.3 Comparison to observations: methodology

In this section we describe the derivation of a number of observables that we use to differentiate and validate our feedback models.

3.3.1 The matter power spectrum and the A_{mod} model

We calculate the 3D matter power spectrum, $P_{\rm m}(k)$, using the routines of Pylians (Villaescusa-Navarro 2018). We first calculate the overdensity field, $\delta(x) = \rho(x)/\bar{\rho}(x) - 1$, on a discrete Cartesian grid with 512^3 pixels for boxes with side length $40 h^{-1}$ Mpc and 1024^3 pixels for boxes with sides of $100 h^{-1}$ Mpc. Taking the coordinates in the simulation snapshots, we assign gas cells, black holes, stars, and dark matter particles to the grid via the first-order linear cloud-in-cell (CIC) scheme, weighting by their mass. Using fast Fourier transforms the Fourier modes of the density contrast field are computed, $\delta(k)$, and the effect of the smoothing from the CIC

kernel is deconvolved. The power spectrum is then calculated as the mean power per k-mode, $P_m(k) = \langle |\delta(k)|^2 \rangle$. To clearly isolated the effect of 'baryonic feedback' on the power spectrum, we calculate the ratio of the full matter power spectrum to the dark-matter-only case, $P_{\rm m}(k)/P_{\rm DMonly}(k)$, where $P_{\rm DMonly}(k)$ is the power spectrum computed on a gravity-only FABLE box with identical initial conditions and box size to that used to calculate $P_{\rm m}(k)$.

The prediction for extreme suppression of the non-linear matter power spectrum as a viable solution to the S_8 tension was first proposed by Amon & Efstathiou (2022) and Preston et al. (2023) using a phenomenological model, A_{mod} . In this simple model, the amplitude of the non-linear power spectrum is modified by the parameter A_{mod} according to

$$P_{\rm m}(k,z) = P_{\rm m}^{\rm L}(k,z) + A_{\rm mod}[P_{\rm m}^{\rm NL}(k,z) - P_{\rm m}^{\rm L}(k,z)], \tag{7}$$

where the superscripts L and NL refer to the linear and nonlinear power spectra, respectively, with the latter assuming CDM cosmology. We refer to this model throughout this work in our assessment of the plausibility of more extreme AGN feedback.

3.3.2 GSMF calculation

In our simulation boxes, we define a galaxy as a subhalo found by the SUBFIND algorithm (Davis et al. 1985; Springel et al. 2001; Dolag et al. 2009), which has more than 100 star particles. Defining the total stellar mass of the simulated galaxy as the sum of all the star particles bound to the subhalo can overestimate the GSMF at the high-mass end (for further details see e.g. Henden et al. 2018). As a result, in this work we follow Genel et al. (2014) and define the galaxy stellar mass as that measured within twice the stellar half-mass radius of the subhalo, as given in the Subfind catalogue. Note that following Henden et al. (2018), when comparing to observations, for all stellar masses we assume a Chabrier (2003) initial mass function (IMF). which involves subtracting 0.25 dex for a Salpeter (1955) IMF and 0.05 dex for a Kroupa (2001) IMF.

3.3.3 Quasar luminosity function calculation

For black holes in radiatively efficient regime we calculate the bolometric luminosities of black holes in our simulation boxes, L_{bol} , according to equation (2). As, for example, discussed in Churazov et al. (2005), the radiative luminosity of AGN accreting at low $f_{\rm BH}$,

3212 L. Bigwood et al.

i.e. those in the radio-mode, may be significantly lower than the values obtained by naively using equation (2).

We therefore explore the impact on the quasar luminosity function (QLF) of distinguishing radiatively efficient and radiatively inefficient AGNs. AGNs with $f_{\rm BH} \geq 0.01$, i.e. those in the quasar-mode in FABLE, have bolometric luminosities calculated following equation (2). For AGNs with $f_{\rm BH} < 0.01$, we follow Churazov et al. (2005) and Habouzit et al. (2022), and approximate the bolometric luminosities as follows:

$$L_{\text{bol}} = 10 f_{\text{BH}} \epsilon_r \dot{M}_{\text{BH}} c^2 \,. \tag{8}$$

We use a linear spline to smooth the transition region in $f_{\rm BH}$ between the two regimes. By comparing bolometric luminosities calculated with this distinction to those calculated under the assumption that all AGNs are radiatively efficient, we aim to somewhat bracket the viable range of the QLF predicted by our models in comparison to observations.

3.3.4 Gas and stellar mass fractions calculation

To calculate the mass fractions, we select groups and clusters as haloes found using the FoF algorithm with mass $M_{500} > 10^{12} {\rm M}_{\odot}$. We define M_{500} as the mass contained within a sphere of radius r_{500} , centred on the minimum potential of the halo, where the mean density is $500 \times$ the critical density of the Universe. The vast majority of gas fraction measurements in the literature are derived from X-ray emission from hot diffuse gas. Therefore, to compare our simulated results with these observations, we follow the approach of Henden et al. (2018) by excluding gas cells with a temperature below $T < 3 \times 10^4$ K and those above the density threshold required for star formation, thereby assuming their contribution to the X-ray emission is negligible. We measure both gas and stellar masses within r_{500} , selecting cells within this radius using a K-D tree algorithm.

3.3.5 X-ray scaling relations calculation

We use the ICM's bolometric luminosity in combination with other global cluster properties to derive the X-ray scaling relations. We take a more simplistic approach to that used in Henden et al. (2018), which involved the generation of mock X-ray spectra to derive X-ray luminosities. We follow Rybicki & Lightman (1985) to estimate the hot ICM X-ray luminosity measured within r_{500} , $L_{500}^{\rm bol}$. The bremsstrahlung emissivity density $\epsilon^{\rm ff}$ is given as

$$\epsilon^{\text{ff}} = 1.4 \times 10^{-27} T^{1/2} n_e n_i Z^2 g_{\text{B}} (\text{ergs}^{-1} \text{cm}^{-3}),$$
 (9)

where T is the gas temperature, n_e and n_i are the electron and ion number densities, respectively, and $g_B = 1.2$ is the average Gaunt factor. Assuming a fully ionized primordial plasma so that $n_e n_i \approx 1.4 \rho^2/(\mu m_p)^2$, we arrive at

$$L_{500}^{\text{bol}} = \frac{2.35 \times 10^{-27}}{\mu^2 m_p^2} \sum_{i}^{r_{500}} m_i \rho_i T_i^{1/2} (\text{erg s}^{-1}),$$
 (10)

where m_i , ρ_i , and T_i are the mass, density, and temperature of *i*th gas cell, m_p is the proton mass, and $\mu = 0.59$ is the mean molecular weight.

We investigate the X-ray scaling relations between L_{500}^{bol} , M_{500} , the gas mass within r_{500} , M_{gas} , and the mass-weighted mean temperature within r_{500} , $T_{500,\text{mw}}$. We note that $T_{500,\text{mw}}$ differs from the characteristic temperature of equation (14). As with gas mass fractions, since we are comparing to X-ray observations from hot diffuse gas, we measure these quantities in the simulations using

only the hot and non-star-forming gas, following the cuts described in Section 3.3.4. Following Henden et al. (2019), we make an additional cut excluding gas cells with a temperature greater than four times the virial temperature, i.e. $k_bT < 4GM_{200}\mu m_p/2r_{200}$. This upper threshold aims to exclude the AGN-driven bubbles created by the radio-mode feedback model, which would contribute excessively high-temperature gas to the scaling relations if a recent strong feedback event had occurred. The simplistic radio-mode model does not capture non-thermal pressure support within bubbles, which means in observations the bubbles should not contribute to the scaling relations until thermalization has occurred. Removing the artificially hot gas created by the feedback model thus reduces bias with respect to the observations.

Finally, we compute the X-ray proxy of the tSZ Compton Y_{500} parameter, Y_X (Kravtsov, Vikhlinin & Nagai 2006). Y_X is the product of the mean X-ray spectroscopic temperature of a cluster and the gas mass measured within r_{500} , and is thus sensitive to the cluster's total thermal energy. We approximate the spectroscopic temperature as $T_{500,\text{mw}}$. Following appendix B2 of Henden et al. (2018), which finds no systematic offset between temperatures derived from X-ray spectra versus mass-weighted temperatures, we calculate Y_X as

$$Y_X = T_{500,\text{mw}} M_{\text{gas}}$$
 (11)

As above, we exclude the cold and star-forming gas (Section 3.3.4), in addition to the high-temperature AGN-driven bubbles.

3.3.6 Thermal Sunyaev–Zel'dovich Compton Y parameter calculation

The thermal Sunyaev–Zel'dovich effect probes the line-of-sight integrated electron pressure, P, and is typically parametrized via the Compton Y_{500} parameter;

$$D_a^2(z)Y_{500} = \frac{\sigma_T}{m_e c^2} \int_0^{r_{500}} P \, \mathrm{d}V \,, \tag{12}$$

where $D_a^2(z)$ is the angular diameter distance of the cluster, σ_T is the Thomson cross-section, and m_e is the electron mass. The quantity integrates the electron pressure in r_{500} , thus providing a measure of the cluster's thermal energy.

We compare the simulation computed Y_{500} – M_{500} relation with Planck Collaboration XI (2013) results, as well as the Wang et al. (2016) re-analysis, which uses weak-lensing calibrated halo masses. To facilitate comparison to the observations, we scale Y_{500} to a fixed angular diameter distance of 500 Mpc. Furthermore, the Planck Collaboration XI (2013) analysis integrates the tSZ flux within a projected circular aperture of radius $5r_{500}$ (giving $Y_{5r_{500}}$), rather than r_{500} . In their analysis a conversion of $Y_{500} = Y_{5r_{500}}/1.796$ was thus applied, which assumes the universal pressure profile of Arnaud et al. (2010) as the spatial template in their matched filter. Since the Arnaud et al. (2010) profile is not well constrained at $5r_{500}$, we avoid the dependency on the assumed modelling choices used in the Planck Collaboration XI (2013) analysis when deriving the inferred Y_{500} from $Y_{5r_{500}}$, and follow Henden et al. (2018) in measuring the Y parameter directly within $5r_{500}$ in the simulation boxes. We revert the Y_{500} measurements of Planck Collaboration XI (2013) back to $Y_{5r_{500}}$ with the 1.796 multiplicative factor.

3.3.7 The ICM profiles calculation

To calculate the electron density, n_e and temperature, T, for groups and clusters in our simulation boxes, for a given halo, we select gas

cells within $3r_{500}$ and divide the gas cells into 10 concentric logarithmically spaced radial bins. We calculate the volume-weighted mean electron density, n_e , and mass-weighted mean temperature, T. Since ICM profiles in literature are typically derived from X-ray observations of hot and dilute plasma, we make the same exclusions of gas cells as described in Section 3.3.4, i.e. ensuring gas cells have $T > 3 \times 10^4$ K and zero star formation rate. In the volume-weighted case, we take the total volume of the bin as the sum of the gas cell volumes, in order to account for the exclusion of gas cells due to the temperature and star formation rate cut. To calculate pressure, P, and entropy, K, radial profiles, we take the product of individual halo $n_e(r)$ and T(r) profiles according to

$$P(r) = k_{\rm B} n_e(r) T(r)$$
 and $K(r) = k_{\rm B} T(r) / n_e^{2/3}(r)$, (13)

where $k_{\rm B}$ is the Boltzmann constant. To allow for comparison between haloes of different mass, we normalize the temperature, pressure, and entropy profiles by the 'characteristic' quantities T_{500} , P_{500} , and K_{500} . T_{500} is defined as

$$T_{500} = \mu m_{\rm p} G M_{500} / 2r_{500} \,, \tag{14}$$

 K_{500} is defined as

$$K_{500} = k_{\rm B} T_{500} / n_{\rm e,500}^{2/3} \,, \tag{15}$$

with $n_{\rm e,500}=500\,f_{\rm b}\rho_{\rm c}(z)/\mu_{\rm e}m_{\rm p}$, where $f_{\rm b}=\Omega_{\rm b}/\Omega_{\rm m}$ and $\rho_{\rm c}=3(100h)^2/8\pi\,G$ are the cosmological baryon fraction and critical density corresponding to our simulation cosmology, respectively, and $\mu_{\rm e}=1.14$ is the molecular weight per free electron. P_{500} is defined as

$$P_{500} = k_{\rm B} n_{\rm e,500} T_{500} \,. \tag{16}$$

4 EXPLORING AGN FEEDBACK IN FABLE-LIKE SIMULATION MODELS

In Section 2, we demonstrated that although many independent hydrodynamical simulations can attain suitable fits to measured GSMF and hot gas fractions in groups and clusters, the predicted matter power spectrum suppression from 'baryonic feedback' can vary significantly. This raises the question: what is the maximum amount of non-linear suppression one can obtain in a hydrodynamical simulation while still maintaining good agreement with the observations?

To address this issue, we ran over 40 different FABLE-like $(40\ h^{-1}{\rm Mpc})^3$ simulation boxes, modifying various aspects of the AGN feedback model in order to study the resultant power spectrum suppression and compare to a number of galaxy, group and cluster observations. The AGN feedback parameters utilized for the full set of simulation boxes are listed in Table B1. We select four illustrative AGN feedback models to discuss throughout the remainder of the work. These are the named boxes in Table B1, i.e. QuasarBoostz2-40, RadioBoost-40, RadioBoost $M_{\rm BH,radio}$ -40 and, XFABLE. In the following sections, we detail the motivation and modifications made to the fiducial FABLE AGN feedback model for each of these variations.

4.1 QuasarBoostz2-40: a quasar-mode boost before cosmic noon

First, we boost the quasar-mode at high redshift by increasing the dimensionless parameter α and the feedback coupling efficiency ϵ_f at z>2. Increasing α will result in a given black hole accreting at a greater rate (equation 1), up to the Eddington limit, powering a quasar with a larger bolometric luminosity and thus allowing

more feedback energy to be available (equation 3). Increasing ϵ_f results in a greater fraction of a quasar's bolometric luminosity being converted to thermal energy (equation 3). Given that the AGN feedback model in FABLE was calibrated on the observed GSMF and hot gas fractions in groups and clusters, one may expect that naive boosts to these parameters would result in poor agreement between the simulations and observations. Certainly, significantly increasing the thermal heating in the centre of galaxies would overquench star formation and drive more powerful outflows reducing the hot gas fraction.

It is important to note however that FABLE is calibrated to data at z = 0. Observationally measured properties of hot haloes in groups and clusters (especially with masses comparable to FABLE objects) become sparse with increasing redshift, particularly beyond cosmic noon at $z \sim 2$. We therefore test boosting both α and ϵ_f by a factor of 100 for z > 2 while resetting parameters to their fiducial values $\alpha = 100$ and $\epsilon_f = 0.1$ at z < 2. We keep all other model parameters, including those associated with the radio-mode, at their fiducial FABLE values. The threshold redshift of z = 2 is chosen as it approximately corresponds to the peaks in star formation rate and black hole growth (Madau & Dickinson 2014). Furthermore, the large boost of a factor of 100 is chosen to exemplify the interplay between the maximum attainable matter power spectrum suppression and the damage to the GSMF and hot gas fractions. As noted in Section 2.1, the DES Y3 redshift distribution peaks at z = 0.4, meaning it is at this redshift that a greater matter power spectrum suppression is observed. Our modification could allow a more destructive feedback scenario, which produces a greater matter power spectrum suppression at $z \ge 0.4$, yet allow galaxy, group, and cluster properties to recover by $z \sim 0$, remaining in good agreement with current observations, which is qualitatively in line with the galaxy cluster the pre-heating scenario (see e.g. Borgani et al. 2001; Voit et al. 2003). We note, however, that even if this feedback model successfully reproduces z = 0 group and cluster properties, remnants of the extreme feedback may persist in the hot CGM, or be visible in the CGM of $z \sim 2-4$ progenitors of present-day galaxy groups and clusters. Such remnants would act as a useful diagnostic tool to constrain AGN feedback models and assess the plausibility of our enhanced feedback model. It is therefore crucial that the model also reproduces CGM properties, as discussed in Section 5.3.3 (see also Lau et al. 2025 for a comparison of simulation models with the observations of Zhang et al. 2024a; b).

4.2 RadioBoost-40: a high-redshift boost to the radio-mode

Next, we consider modifications to the radio-mode AGN feedback. We note that the matter power spectrum suppression required by the A_{mod} and WL + kSZ models to resolve the S_8 tension shows the greatest discrepancy with FABLE and other hydrodynamical simulations in the mildly non-linear regime of $k \sim 1 h \, \mathrm{Mpc}^{-1}$ (see the left panel of Fig. 1), corresponding to relatively large spatial scales of ~ 10 Mpc at z = 0. This indicates that AGN feedback would be required to impact the matter distribution at greater distances from the central black hole than currently occurs in the FABLE model. Motivated by this, our first radio-mode modification involves injecting the hot radio-mode bubbles at a greater distance from the black hole by increasing the D_{bub} parameter. This mimics bubbles arising from AGN jets, which have travelled further through the intervening ICM. This qualitatively shares some similarities with the hydrodynamical decoupling of AGN jets in the SIMBA model (Davé et al. 2019), although the exact details of the implementation are considerably different.

3214 L. Bigwood et al.

A major increase of $D_{\rm bub}$ from its fiducial value at $z\sim 0$ would be expected to reduce the hot gas fraction measured within r_{500} , and possibly result in a poorer fit to the data. We therefore follow a similar approach to the previous Section 4.1 and trial a redshift-dependent $D_{\rm bub}$. We test increasing $D_{\rm bub}$ at high redshifts, with the aim of redistributing matter on the larger scales and thus suppressing the mildly non-linear matter power spectrum. We then decrease $D_{\rm bub}$ with redshift at late time, with the purpose of ensuring gas can reaccrete and allow the simulated gas fractions to attain good agreement with low-redshift observations.

The RadioBoost-40 simulation demonstrates this model. At z > 4 we fix $D_{\text{bub}} = 500 \ h^{-1}$ kpc. From z = 4 to z = 0 we then decrease D_{bub} linearly with redshift until it reaches the value of $D_{\text{bub}} = 30 \ h^{-1}$ kpc at z = 0. We fix the bubble radius R_{bub} to its fiducial normalization value of $50 \ h^{-1}$ kpc. Note that we therefore remove the re-scaling of D_{bub} and R_{bub} with the bubble energy and ICM density, given in equation (5) and equation (6), to have more control over the model. Furthermore, to increase the proportion of black holes undergoing feedback in this modified radio-mode, we increase χ_{radio} to 0.1. We keep all other aspects of the model, including the quasar-mode, as in fiducial FABLE.

4.3 RadioBoostM_{BH,radio}-40: a boost to the radio-mode for the most massive SMBHs

The next modified AGN feedback model we test builds on the modifications to the radio-mode outlined in the previous Section 4.2. We discussed that increasing the matter power spectrum suppression on the larger mildly non-linear scales could be possible through an increase to the distance that the hot 'AGN jet-driven' bubbles are injected at from the black hole. We however cannot guarantee that gas can re-accrete sufficiently in late times to recover observed gas fractions while maintaining the larger scale power spectrum suppression we desire. In this section, we therefore consider an alternate approach.

The box exemplifying our new approach is labelled 'RadioBoost $M_{\rm BH,radio}$ -40'. First, we increase the bubble distance to $D_{\rm bub}=100~h^{-1}$ kpc at all redshifts. Furthermore, we allow the radio-mode to act in only the largest haloes, motivated by the aim of preserving reasonable gas fractions in (small) groups, where feedback-induced gas expulsion occurs more easily for the lower mass systems with smaller binding energies. It has been shown that above a stellar mass of $10^{11}~M_{\odot}$, radio-loud AGNs are possibly always 'switched on' (see Hardcastle & Croston 2020 and references therein). This also approximately corresponds to the threshold halo mass for which a sufficiently dense hot halo is in place such that it can confine the radio bubbles and ensure that a sufficient fraction of energy from bubbles can be transferred to the ICM.

We therefore allow radio-mode feedback to operate only in haloes that have a considerable 'hot halo' component, corresponding roughly to $M_{500}\approx 10^{13}~{\rm M}_{\odot}$, $\log_{10}(M_*[{\rm M}_{\odot}])\approx 11$ (using the best-fitting Moster et al. 2010 stellar mass-halo mass relationship), and $\log_{10}(M_{\rm BH}[{\rm M}_{\odot})\approx 9$ (using the best-fitting Kormendy & Ho 2013 stellar mass-black hole mass scaling relation). We retain the $\chi_{\rm radio}=0.1$ of the previous section, and allow only haloes accreting below this limit and with black hole mass $\log_{10}(M_{\rm BH}[{\rm M}_{\odot}])>9$ to be in the radio-mode. Black holes of mass $\log_{10}(M_{\rm BH}[{\rm M}_{\odot}])<9$ are only allowed to undergo quasar-mode feedback, regardless of their accretion rate. This model has some qualitative similarities to the adopted separation between the quasar and radio-mode in the IllustrisTNG simulation (Weinberger et al. 2018), but

note that quantitative details and radio-mode implementation are different.

4.4 XFABLE: a pressure-limited boosted radio-mode for the most massive SMBHs

Finally, we consider an additional modification to the 'RadioBoost $M_{\rm BH, radio}$ -40' model described in the previous section. The modifications to the fiducial FABLE radio-mode described thus far do not address the energy transferred to the ICM by the injected radio bubbles. In fact, in fiducial FABLE there is no physical cap on the pressure contrast between the inflating bubble and the ICM. This can result in high Mach number shocks that are not typically observed around X-ray cavities (see Fabian 2012, for a review). Furthermore, dedicated high-resolution simulations of jets in galaxy clusters typically find that they are inflated in approximate pressure equilibrium (Hardcastle & Krause 2013; Bourne & Sijacki 2021). Considering that the 'RadioBoost $M_{\rm BH,radio}$ -40' model may result in a more destructive feedback scenario since bubbles are injected further from the central black hole, we test additionally applying an upper limit on the energy of the bubble with respect to the ICM. The box that exemplifies this modification is labelled 'XFABLE', in which we ensure the energy content of the bubble is limited to $E_{\text{bub}}/E_{\text{ICM}} < 20$. This limit was chosen through a series of trial runs, with the aim of achieving a balance between injecting sufficient energy into the ICM to suppress the matter power spectrum and preventing thermodynamic profiles of the ICM deviating significantly from observations.

In addition to the $(40 \ h^{-1}\text{Mpc})^3$ volume ran with this model (XFABLE-40), we additionally run a $(100 \ h^{-1}\text{Mpc})^3$ box for improved statistics of rare systems (XFABLE-100).

4.5 Visualization of the FABLE simulation suite

Fig. 2 shows visualizations of the z=0 large-scale structure formed in each of the simulation boxes introduced in this section. Since the $(40\ h^{-1}{\rm Mpc})^3$ and $(100\ h^{-1}{\rm Mpc})^3$ boxes were ran with the same random seed for the initial conditions, we find that the cosmic web looks comparable between the volumes, with the largest clusters lying at approximately the same relative location between boxes. The $(100\ h^{-1}{\rm Mpc})^3$ boxes however allow for rarer objects to form, with the three most massive clusters in FABLE-100 being of mass $M_{500}=4.05\times10^{14}\ {\rm M}_{\odot}, 3.89\times10^{14}\ {\rm M}_{\odot}, 3.20\times10^{14}\ {\rm M}_{\odot}, {\rm compared to}\ M_{500}=1.46\times10^{14}\ {\rm M}_{\odot}, 1.01\times10^{14}\ {\rm M}_{\odot}, 4.59\times10^{13}\ {\rm M}_{\odot}$ in FABLE-40.

The surface gas mass density of the FABLE-100 and XFABLE-100 volumes look largely similar, albeit with XFABLE-100 displaying somewhat lower densities at the nodes. In the $(40 h^{-1} \text{Mpc})^3$ volumes we see greater variation in the surface gas density distribution between AGN feedback models. In particular, the RadioBoost-40 and RadioBoostM_{BH,radio}-40 visualizations reveal a more 'fuzzy' gas distribution, with less defined filaments and nodes than fiducial FABLE-40. This largely arises from the choice of increased D_{bub} parameter in these AGN feedback models, which redistributes gas to larger distances from the central SMBH. The mass-weighted temperature projections further display the extremity of hot gas redistribution imposed by the RadioBoost-40 and RadioBoostM_{BH,radio}-40 models. The temperature projections also reveal clear deviations between the FABLE and XFABLE models, most notably that bubbles of hot gas around the largest clusters reach greater radii in XFABLE.

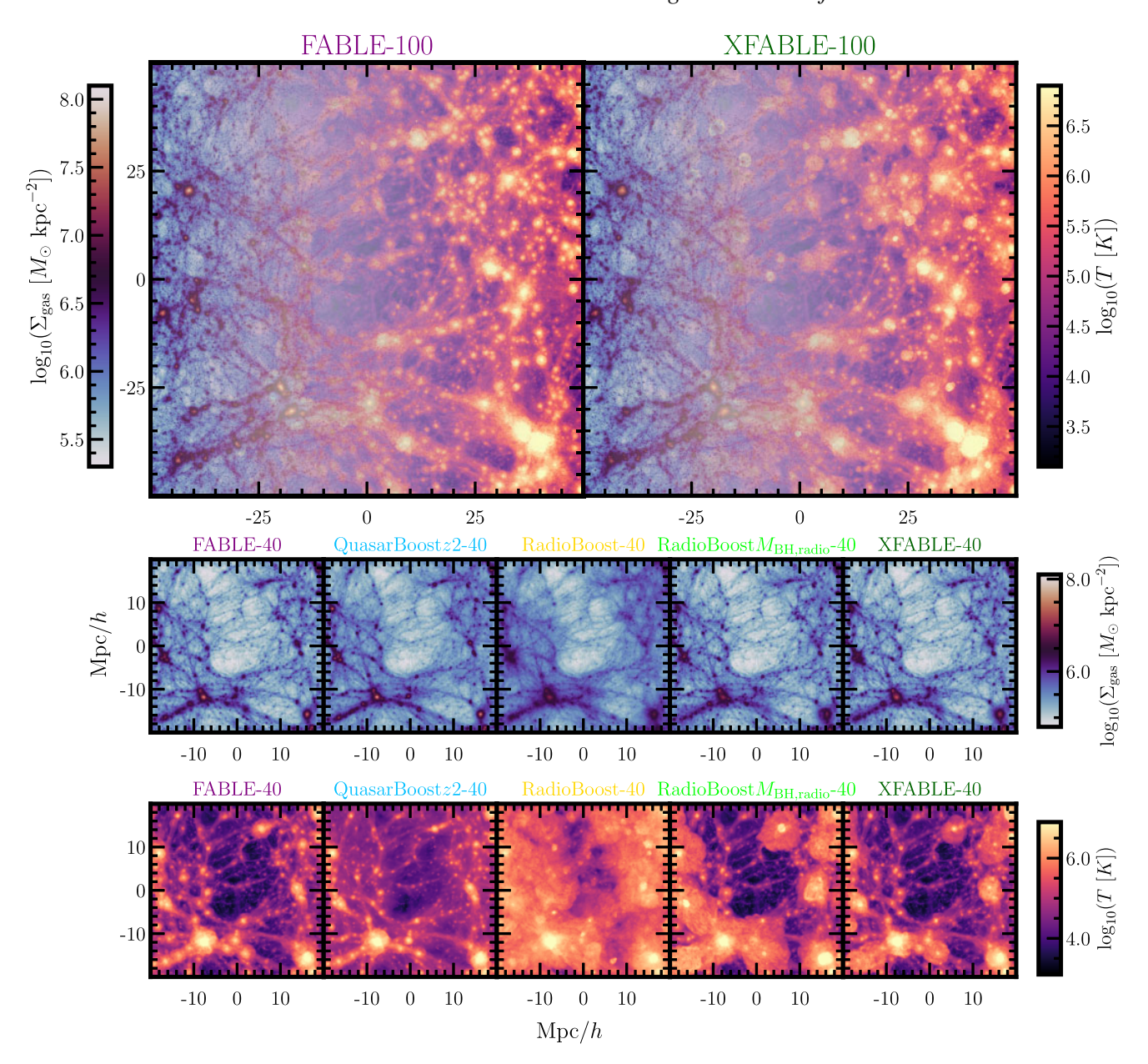


Figure 2. Projections visualizing the key simulation boxes analysed in this work. The top panels display the blend of the gas surface density and mass-weighted temperature projections of the two $(100 \ h^{-1}\text{Mpc})^3$ volumes: fiducial FABLE-100 and the modified AGN feedback model, XFABLE-100. The middle panels show the gas surface density of the corresponding $(40 \ h^{-1}\text{Mpc})^3$ FABLE-40 and XFABLE-40 boxes, in addition to the other modified AGN feedback models; QuasarBoostz2-40, RadioBoost-40, and RadioBoost $M_{BH,radio}$ -40. The lower panels show mass-weighted temperature projections for the same $(40 \ h^{-1}\text{Mpc})^3$ volumes. All visualizations represent projections through the full depth of each simulation box at z = 0.

5 CONSTRAINING AGN FEEDBACK MODELS THROUGH COMPARISON WITH OBSERVATIONS

In this section, we test the ability of the models outlined in the previous section to reproduce a range of observed galaxy, SMBH, galaxy group, and galaxy cluster properties. We discuss models that can be ruled out as viable modifications to the FABLE feedback model, as well as the constraining power of specific observations to distinguish and/or exclude our theoretical models. Throughout Section 5, we plot results from $(40\ h^{-1}{\rm Mpc})^3$ boxes using dashed lines and from the $(100\ h^{-1}{\rm Mpc})^3$ FABLE and XFABLE boxes using solid lines. Observational measurements are shown in grey.

5.1 The suppression of the matter power spectrum

We begin by discussing the baryonic suppression of the matter power spectrum with respect to a dark-matter-only simulation, as predicted by FABLE and each of the modified feedback boxes. Fig. 3 shows the suppression at z=0,1,2 and at z=0.4, with the latter redshift plotted for comparison to the $A_{\rm mod}$ model, which we recall is the model required to produce enough suppression to be a viable solution to the S_8 tension (see Section 2.1). We also plot at z=0.4 $A_{\rm mod}$ binned in k-space, A_i , to highlight the scale-dependence of the suppression (Preston et al. 2023). At z=0 we also compare to the constraints attained by the combined weak lensing and kSZ (WL + kSZ) analysis presented in Bigwood et al. (2024) (purple band). These constraints were computed at z=0, in contrast to the

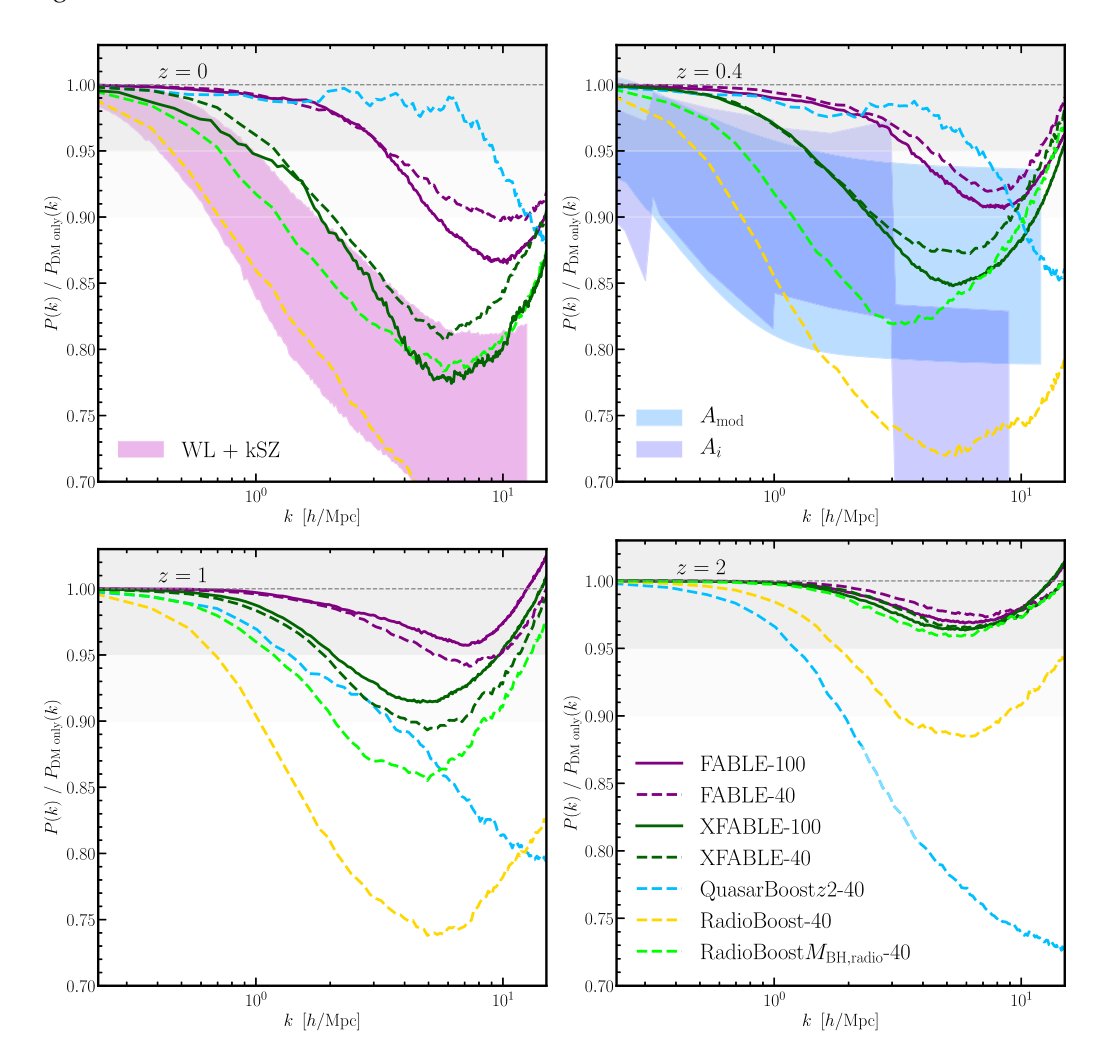


Figure 3. The matter power spectrum suppression due to baryonic effects measured in each of our key simulation boxes, plotted at z=0 (upper left), z=0.4 (upper right), z=1 (lower left), and z=2 (lower right). The dashed lines denote $(40 \, h^{-1} {\rm Mpc})^3$ boxes, and the solid lines show $(100 \, h^{-1} {\rm Mpc})^3$ boxes. We show the fiducial FABLE boxes (purple) and our key modified AGN feedback models; QuasarBoostz2-40 (light blue), RadioBoost-40 (yellow), RadioBoost $M_{\rm BH, radio}$ -40 (light green), and XFABLE (dark green). At z=0 we plot as the purple shaded region the constraints attained in a combined DES Y3 cosmic shear and ACT kSZ (WL + kSZ) analysis, presented in Bigwood et al. (2024). At z=0.4 we plot as the light blue shaded region the $A_{\rm mod}=0.858\pm0.052$ constraints of Preston et al. (2023) required to reconcile cosmology attained in a DES Y3 cosmic shear analysis with the *Planck* best-fitting ΛCDM model. The dark blue shaded region shows the corresponding 1σ constraints when splitting the model into bins in wavenumber, A_i .

constraints attained using the $A_{\rm mod}$ model, which has no explicit redshift dependence, and hence is plotted at $z \sim 0.4$ where the total DES Y3 redshift distribution peaks.

In line with Martin-Alvarez et al. (2024), we find that the suppression produced by the fiducial FABLE boxes (purple) increases with time, with the suppression pushing to larger k-scales and a greater amplitude with decreasing redshift. This trend is observed in each of the modified feedback boxes, with the exception of QuasarBoostz2-40 (light blue). In this model, the high-redshift quasar-mode boost, and thus the increased thermal energy supplied to the gas, has significantly increased the power suppression at z = 2 with respect to fiducial FABLE, as expected. Specifically, at $k = 10 h \, \mathrm{Mpc}^{-1}$ the suppression increases from ~ 2 per cent to ~ 25 per cent in QuasarBoostz2-40, and interestingly produces suppression on scales as large as $k \sim 0.5 h \, {\rm Mpc^{-1}}$. We, however, find that the power suppression decreases in the QuasarBoostz2-40 model beyond z < 2, and produces less suppression than fiducial FABLE on scales 1 h Mpc⁻¹ < k < 10 h Mpc⁻¹ at z < 0.4. Furthermore, the box is unable to reproduce the A_{mod} suppression required at z = 0.4, and therefore this modification to the AGN feedback model cannot provide a solution to the S_8 tension, hinting at a need for sufficiently strong AGN feedback at lower redshifts as well.

The models RadioBoost-40 (yellow), RadioBoostM_{BH,radio}-40 (light green), and XFABLE (dark green) are all able to produce a greater non-linear suppression of the matter power spectrum than fiducial FABLE for 0.1 $h \, \text{Mpc}^{-1} < k < 10 \, h \, \text{Mpc}^{-1}$ at 0 < z < 2. In particular, RadioBoost-40 predicts the most extreme baryonic impact of all illustrative models shown, and at z = 0 suppresses the power spectrum by ~ 25 per cent at $k = 3 h \, \mathrm{Mpc}^{-1}$ (compared to a ~ 5 per cent suppression in the fiducial FABLE box). It lies consistent with both the A_{mod} and A_i models at z = 0.4, and the constraint attained from a weak lensing and kSZ combined analysis at z = 0(Bigwood et al. 2024). Since the RadioBoost $M_{\rm BH,radio}$ -40 model restricts a 'boosted' radio-mode to act for only the most massive black holes in the box, we inevitably find that this model predicts a less extreme suppression at all k than RadioBoost-40, at z = 0suppressing the power spectrum by ~ 17 per cent at $k = 3 h \, \mathrm{Mpc}^{-1}$. RadioBoost $M_{\rm BH,radio}$ -40 is however still able to lie within both the

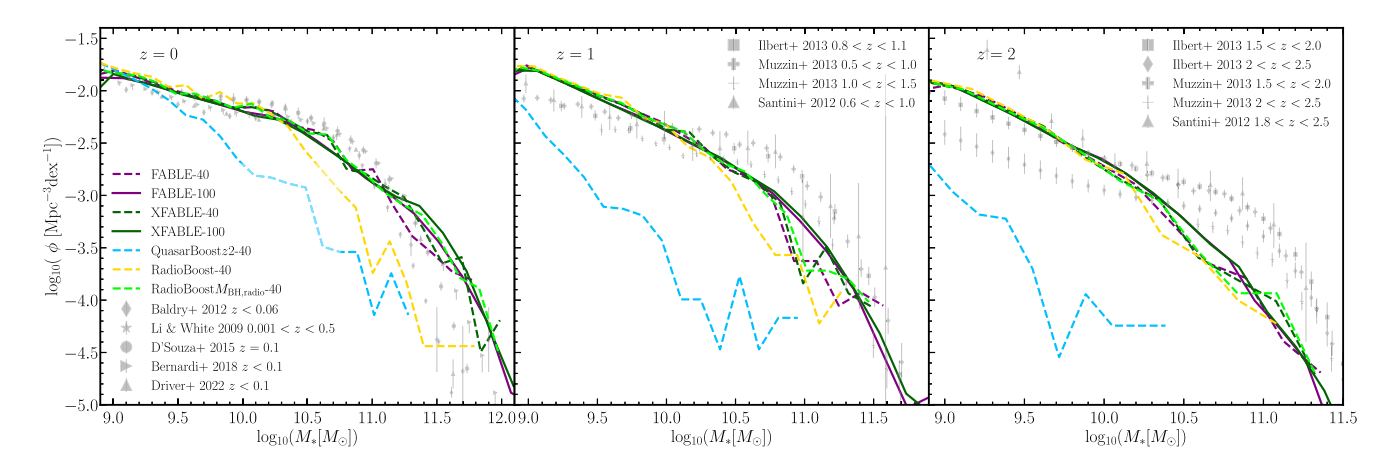


Figure 4. The GSMF measured within twice the stellar half-mass radius in each of our key simulation boxes, plotted at z=0 (left), z=1 (centre), and z=2 (right). The dashed lines denote $(40 \ h^{-1} \text{Mpc})^3$ boxes, and the solid lines show the $(100 \ h^{-1} \text{Mpc})^3$ FABLE and XFABLE boxes. We show the fiducial FABLE boxes (purple) and our key modified AGN feedback models; QuasarBoostz2-40 (light blue), RadioBoost-40 (yellow), RadioBoost $M_{\text{BH,radio}}$ -40 (light green), and XFABLE (dark green). The grey data points show observational constraints. At z=0 we plot the results of Baldry et al. (2012) (z<0.06), Li & White (2009) (0.001 < z < 0.5), D'Souza et al. (2015) (z=0.1) Bernardi et al. (2018) z<0.1), and Driver et al. (2022) (z<0.1). At z=1 we plot Ilbert et al. (2013) (0.8 < z < 1.1), Muzzin et al. (2013) (plotting both 0.5 < z < 1.0 and 1.0 < z < 1.5), and Santini et al. (2012) (0.6 < z < 1.0). Similarly at z=2 we plot Ilbert et al. (2013) (plotting both constraints for 1.5 < z < 2.0 and 2.0 < z < 2.5) and Santini et al. (2013) (plotting both constraints for 1.5 < z < 2.0 and 2.0 < z < 2.5) and Santini et al. (2013) IMF. We show that XFABLE remains an equally good fit to the observations as FABLE, and that the QuasarBoostz2-40 and RadioBoost-40 boxes are ruled out by the data.

 $A_{\rm mod}$ and WL + kSZ bands. The additional pressure limit on the AGN bubbles imposed in the XFABLE box further reduces the suppression measured at all k and z shown. XFABLE attains a z=0 suppression of ~ 13 per cent at $k=3\,h\,{\rm Mpc}^{-1}$, approximately 2.5 greater than measured in FABLE. This brings XFABLE to lie within the 1σ WL + kSZ constraints of Bigwood et al. (2024) at nearly all scales at which we expect the matter power spectrum to be suppressed due to feedback, i.e. within $0.1\,h\,{\rm Mpc}^{-1} < k < 10\,h\,{\rm Mpc}^{-1}$. XFABLE also lies consistently within the 1σ $A_{\rm mod}$ and A_i model predictions at $k\gtrsim 1\,h\,{\rm Mpc}^{-1}$, lying within 2σ at the larger mildly non-linear scales.

The default FABLE and QuasarBoostz2-40 models fail to match the the power suppression constrained by weak lensing and kSZ observations, while the RadioBoost-40, RadioBoost $M_{\rm BH, radio}$ -40, and XFABLE models are consistent with the observations, and the predicted suppression to resolve the S_8 tension. It is interesting to note that our comparison between different AGN feedback models does not favour very strong ejective AGN feedback at cosmic noon or higher redshifts (as advocated by basic pre-heating scenarios), given that there is sufficient cosmic time for this ejected gas to refall back within the galaxy groups and clusters at low redshifts, and hence significantly reduce the suppression of the matter power spectrum where we have the best observational constraints. Instead, AGN feedback that regulates their host properties seems to be required at lower redshifts as well, in accord with the observed presence of radio jets and lobes in local galaxy groups and clusters.

5.2 Galaxy and SMBH population properties

5.2.1 The GSMF

Fig. 4 shows the GSMF at z=0,1, and 2 for FABLE and each of our four illustrative modified AGN feedback models. We compare to observational results measured using data attained from a number of surveys and fields: Baldry et al. (2012) (Galaxy And Mass Assembly, GAMA), Li & White (2009) (Sloan Digital Sky Survey,

SDSS), D'Souza et al. (2015) (SDSS), Bernardi et al. (2018) (SDSS), Driver et al. (2022) (GAMA), Ilbert et al. (2013) (UltraVISTA), Muzzin et al. (2013) (COSMOS/UltraVISTA), and Santini et al. (2012) (Wide Field Camera 3, WFC3). The redshift ranges of the data plotted is shown in the caption. In line with Henden et al. (2018) and by construction, the fiducial FABLE boxes display a very good agreement with the observations at z=0. At z=1 FABLE underestimates the knee of the GSMF compared to the data, and at z=2 the simulated GSMF is systematically lower for $\log_{10}(M_*[M_\odot] > 10.3$ (also seen in Henden et al. 2018), but maintains a broadly good qualitative agreement.

The QuasarBoostz2-40 model provides the poorest fit to the data, significantly underestimating the stellar mass throughout the galaxy population. The boost to the quasar-mode increases thermal energy injected into the central galaxy at z>2, over quenching the star formation predicted at z=2 compared to observations. The GSMF begins to recover towards z=0 with the implementation of the fiducial quasar-mode parameters at z<2 due to gas fallback; however, sufficient stellar mass cannot be formed to match the data at z=0. This strongly indicates (even considering significant changes in the stellar feedback sector) that strong ejective central gas removal due to AGN feedback is disfavoured, generating unrealistic star formation histories of the entire galaxy population.

At $z \le 1$, the RadioBoost-40 model also underestimates the massive tail $(\log_{10}(M_*[M_\odot]) > 10.5)$ of the GSMF. Recall that this model imposes a linearly decreasing bubble distance with redshift, as well as ensuring that more black holes are in the radio-mode at a given time with an increased $\chi_{\rm radio}$. We compare to further observables to diagnose the source of the low GSMF (see Section 5.3.1 and Section 5.3.4).

Both the RadioBoost $M_{\rm BH,radio}$ -40 and XFABLE models are in excellent agreement with the fiducial FABLE simulation and maintain the same level of agreement to observations at z=0, 1, and 2. This indicates that fixing $D_{\rm bub}=100~h^{-1}$ kpc at all times, in addition to allowing the radio-mode to act in only the most massive haloes, is able to prevent the overheating/ejection of gas within the central galaxy and maintain realistic star formation. The addition of the

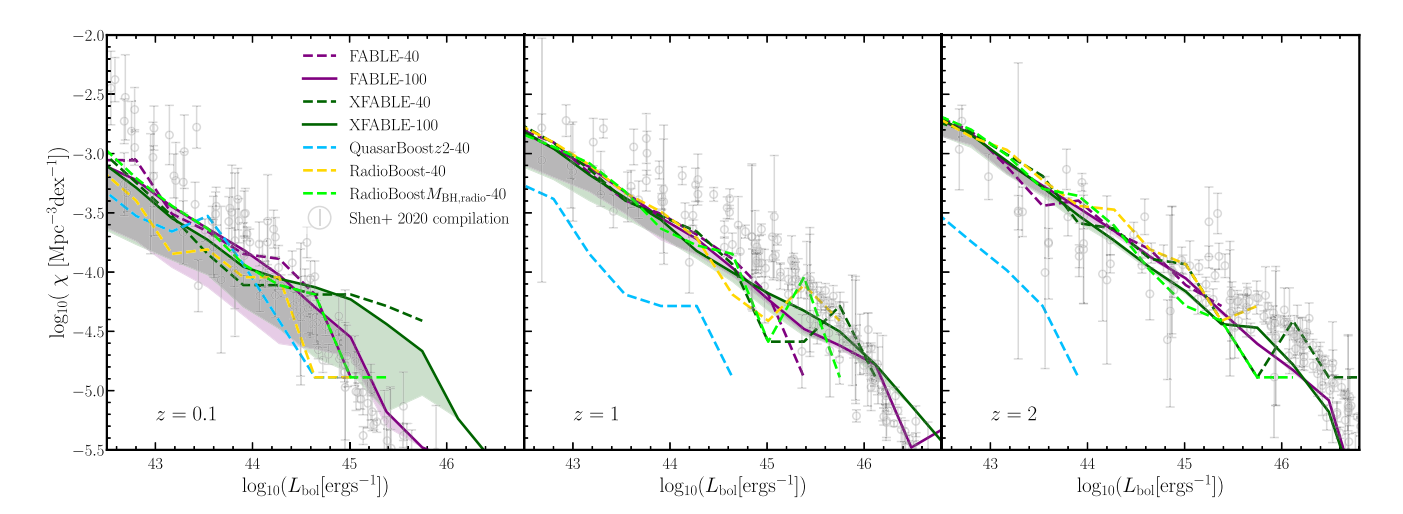


Figure 5. The bolometric QLF for each of our key simulation models, plotted at z = 0.1 (left), z = 1 (centre), and z = 2 (right). The dashed lines denote $(40 \ h^{-1}\text{Mpc})^3$ boxes, and the solid lines show the $(100 \ h^{-1}\text{Mpc})^3$ FABLE and XFABLE boxes. We show the fiducial FABLE boxes (purple) and our key modified AGN feedback models; QuasarBoostz2-40 (light blue), RadioBoost-40 (yellow), RadioBoost $M_{\text{BH,radio}}$ -40 (light green), and XFABLE (dark green). Lines show the QLF computed under the assumption that all AGN are radiatively efficient. For the FABLE-100 and XFABLE-100 boxes, we add a shaded area that brackets the predicted luminosity function spanned by this assumption and that accounting for the radiatively inefficient AGN population at low Eddington ratios (see Section 3.3.3). The grey data points show observational constraints from the Shen et al. (2020) compilation. We demonstrate that the z = 0.1 QLF is robust to the differences in the feedback model we show, but that the QuasarBoostz2-40 model is ruled out at $z \ge 1$.

AGN bubble pressure limit in XFABLE has no appreciable impact on the GSMF, likely because the radio-mode is heating only the outskirts of galaxies and therefore the stellar population remains largely unaffected.

Comparison to observed GSMF can therefore rule out the QuasarBoostz2-40 and RadioBoost-40 models, as they lead to extreme stellar mass overquenching, with the default FABLE, RadioBoost $M_{\rm BH,radio}$ -40, and XFABLE models remaining in good agreement with the data. We conclude from this analysis that any significant variations of the AGN feedback, which could lead to sufficiently large matter power spectrum suppression, need to largely act in galactic outskirts rather than galaxy central regions. Keeping the same stellar feedback model as in FABLE, it seems hard to reconcile the observed matter power spectrum suppression and GSMF data for strong centrally ejective AGN feedback models, hinting that the AGN feedback needs to be largely 'preventative' and/or act on large scales. This point can be made even stronger, by noting that FABLE overquenches galaxies at the massive end at $z \sim 2$, which implies that either stellar and/or AGN feedback acting in galaxy cores at early cosmic times before the cosmic noon is too powerful. Resolving this issue would either require less strong feedback overall at high cosmic times or AGN feedback, which is more 'preventative' and/or ejective but at large distances from galactic centres.

5.2.2 The bolometric QLF

Since quasars are the most luminous non-transient objects in the Universe, they can be detected and characterized to beyond z > 7. As a result, the redshift evolution of the QLF provides a unique window into the growth of the active SMBH population and therefore is a key reference to compare our simulated SMBHs to. We compare our simulated quasar populations against the compilation of observational measurements by Shen et al. (2020), which includes quasar samples measured in the optical/UV, X-ray and infrared bands. Fig. 5 plots the simulated and observed bolometric QLFs at z = 0.1, z = 1, and

z = 2, with the former redshift plotted due to the greater availability of data for comparison at z = 0.1 rather than z = 0.

At z = 0.1, we find a good agreement between each of the modified AGN feedback models, fiducial FABLE, and the observational data. This implies that the number density of low-redshift quasars and their luminosities are relatively robust to the explored changes in AGN feedback prescriptions, and based on the QLF we cannot easily differentiate between models that predict a vastly different suppression of the matter power spectrum. 10 We further note that at the bright end, XFABLE appears to overproduce the number density of the most luminous quasars in the box $(\log_{10}(L_{bol}[erg s^{-1}]) > 45)$ if we naively assume that all SMBHs are radiatively efficient. Accounting for a population of radiatively inefficient accretors at low Eddington ratios with the shaded areas bracketing the predicted FABLE and XFABLE QLFs spanned by the assumption that all AGN are radiatively efficient (as is often assumed in luminosity functions derived from hydrodynamical simulation), and a calculation based on explicitly distinguishing between the luminosities of radiatively efficient and radiatively inefficient AGN (computed as detailed in Section 3.3.3) largely removes this discrepancy, highlighting the importance of accurately computing radiative efficiencies. We finally note that all models somewhat underpredict the z = 0.1 QLF at the faint end $((\log_{10}(L_{\text{bol}}[\text{erg s}^{-1}]) < 43.5)$, which indicates that the observed population is likely accreting more efficiently than in FABLE-like models in lower mass galaxies (we further caveat that we do not model X-ray binaries in this work). This intriguingly points towards a scenario of potentially greater feedback from these low-luminosity AGNs than modelled in the FABLE-like models (see also detailed discussion in Koudmani, Sijacki & Smith 2022). Note

 10 Furthermore, we have analysed $M_{\rm BH}-M_*$ scaling relation for all of our AGN feedback models and compared them to the observationally derived relations of Reines & Volonteri (2015) and Greene, Strader & Ho (2020). Due to the scatter in the available observational data, we find that we cannot exclude any of our modified feedback boxes using the $M_{\rm BH}-M_*$ scaling relation alone.

that the simulated QLFs should be seen in the context of current cosmological hydrodynamical simulations, which show a significant uncertainty in predicting the bolometric QLF (see fig. 5 of Habouzit et al. 2022).

At z>1 each of the radio-mode modifications, i.e. RadioBoost-40, RadioBoost $M_{\rm BH,radio}$ -40, and XFABLE also do not deviate from the prediction by the fiducial FABLE model and agree very well with observational data. Hence, we can further infer that the SMBH's growth is not significantly impacted by the radio-mode bubbles acting far from the galaxy centre at these redshifts. Despite recovering by z=0.1, the QuasarBoostz2-40 model significantly underestimates the QLF at z=1 and z=2. From this, we deduce that the outflows resulting from the increased thermal feedback drive too much gas away from central SMBHs, preventing their growth and therefore reducing the number density of luminous quasars. This same process overquenches the central galaxies as shown in Section 5.2.1.

5.3 Global properties of galaxy groups and clusters

5.3.1 Hot gas mass fractions

The upper left panel of Fig. 6 shows the z=0 hot gas mass fractions in the simulated groups and clusters for each illustrative AGN feedback model, in comparison to observations at $z\sim0$. As in Fig. 1, we plot the gas mass-halo mass of Akino et al. (2022) derived from the XXL X-ray selected sample, using the Hyper Suprime-Cam's photometry and weak-lensing mass measurements. We also plot a range of X-ray observations from Vikhlinin et al. (2006) (*Chandra*), Maughan et al. (2008) (*Chandra* ACIS-I), Croston et al. (2008) (*XMM-Newton* REXCESS), Gonzalez et al. (2013) (*XMM-Newton*), Lovisari et al. (2015) (*XMM-Newton*, selected using the ROSAT Allsky Survey), and Eckert et al. (2016) (XXL-100-GC clusters from *XXM-Newton*). The redshift ranges of the data plotted is shown in the figure caption. We add an arrow to Fig. 6 indicating what would be the likely effect on X-ray-derived observations if one would correct for a hydrostatic mass bias of 30 per cent.

Recently, several observational studies have found evidence that gas mass fractions in group-mass systems may be lower than previous measurements derived using X-ray bright groups. These include the constraints of Popesso et al. (2024), which measure the gas mass fractions in optically selected groups using eROSITA. Their optical selection aims to circumvent the potential biases that previous measurements of X-ray bright groups may have been susceptible to; namely that flux-limited X-ray selected samples can miss groups that have undergone feedback-induced gas removal and therefore have reduced X-ray luminosities. This may result in previous measurements of X-ray bright groups overestimating gas mass fractions in groupmass systems (Popesso et al. 2024). Independently, the joint weak lensing + kSZ analysis of Bigwood et al. (2024) also constrained gas mass fractions in groups to be lower than the existing X-ray measurements. We therefore add these recent constraints to Fig. 6.

In agreement with Henden et al. (2018), the fiducial FABLE-100 box provides a good fit to the observational data points at z=0. We note however that in light of the recent group-mass constraints of Popesso et al. (2024) and Bigwood et al. (2024) favouring lower gas mass fractions than previous measurements, the fiducial FABLE model may require re-calibration to match observations for the least massive groups at $M_{500} \lesssim 2-3 \times 10^{13} \, {\rm M}_{\odot}$. We find that the RadioBoost $M_{\rm BH,radio}$ -40 and XFABLE models also lie within the large scatter of the observations. XFABLE displays a drop in the gas mass fractions at $M_{500} \sim 10^{13} \, {\rm M}_{\odot}$, owing to the simplistic nature of the modified sub-grid implementation of AGN

feedback, which allows the boosted radio-mode to act solely in haloes approximately above this mass¹¹ (see Section 4.4). We note that we also ran a box with an identical model to XFABLE, but with a lower minimum black hole mass at which radio-mode feedback is allowed to occur; decreasing the limit from $\log_{10}(M_{\rm BH}[{\rm M}_{\odot}]) > 9$ to $\log_{10}(M_{\rm BH}[{\rm M}_{\odot}]) > 8.5$ (see Table B1). We found that the impact of allowing lower mass black holes to undergo radio-mode feedback was to lower the gas fractions with respect to XFABLE in haloes with $5 \times 10^{12} \text{ M}_{\odot} \lesssim M_{500} \lesssim 2 \times 10^{13} \text{ M}_{\odot}$, and to cause a greater suppression of the matter power spectrum but only at $k > 2 h \,\mathrm{Mpc}^{-1}$, leaving the suppression on larger scales unchanged. Furthermore, it is also interesting to note that both the RadioBoostM_{BH,radio}-40 and XFABLE models display significantly increased scatter in the predicted hot gas fractions for halo masses $M_{500} \gtrsim 10^{13} M_{\odot}$ due to the more bursty nature of radio-mode, which is able to better reproduce the large observed scatter inferred from X-ray observations.

The RadioBoost-40 model predicts gas fractions up to a factor of 4 smaller than the fiducial FABLE model at z=0, with a constant median gas fraction of $M_{\rm gas,500}/M_{\rm 500}\sim0.01$ across the group population. Since this modified AGN feedback model injects radio bubbles at a greater distance from the central black hole, we can infer that too much gas is ejected beyond $r_{\rm 500}$, placing gas mass fractions at the lower end of observations, especially for the most massive systems present in the box. This effect is amplified by the increased $\chi_{\rm radio}=0.1$, which forces more black holes be in the more efficient radio-mode. We note however that the RadioBoost-40 model is in reasonable agreement with the recent group-mass constraints of Popesso et al. (2024) and Bigwood et al. (2024).

The QuasarBoostz2-40 box lies above fiducial FABLE gas fraction at z=0 and at the very upper end of the observational scatter. As discussed in Section 5.1, at z>2, significantly more thermal energy is supplied close to the black hole, driving powerful outflows that redistribute gas beyond r_{500} and reduce the measured gas fractions. This gas re-accretes only towards z=0, resulting in the higher gas fractions. This model also displays a steeper mass trend than fiducial FABLE, indicating that 'tuned down' quasar feedback at lower redshifts is preferentially unable to prevent gas re-accretion in more massive haloes (see also Martin-Alvarez et al. (2024) for a discussion on the scale dependence of the feedback modes).

The lower left panel of Fig. 6 shows the redshift evolution in the hot gas mass fractions for the same set of simulation models. Here, we calculate the median and the quartiles in the hot gas fractions for the simulated haloes satisfying $M_{500} > 5 \times 10^{12}~{\rm M}_{\odot}$. Unfortunately, currently there are no available observations overlapping with the resolvable range of FABLE group masses to benchmark these models at $z \ge 1$, however we plot the redshift dependence to trace the evolution of gas ejection induced by our AGN feedback model variations. This prediction will turn very useful for the next generation SZ measurements, such as the Simons Observatory.

We find that in the fiducial FABLE box, the gas mass fractions decrease with time from z < 3. This is due to late-time feedback in the radio-mode inducing gas expulsion beyond R_{500} (see Martin-Alvarez et al. (2024) which demonstrated this is the dominant feedback mode at low redshift). This trend is also observed in each of the modified radio-mode boxes; RadioBoost-40, RadioBoost $M_{\rm BH,radio}$ -40 and XFABLE. The RadioBoost $M_{\rm BH,radio}$ -40 and XFABLE boxes

¹¹ High-resolution simulations able to capture relativistic AGN jet propagation and bubble-inflation would self-consistently determine where and in which haloes the jet energy is thermalized, which would naturally lead to a scatter in the gas mass fraction relation, without introducing any sharp features.

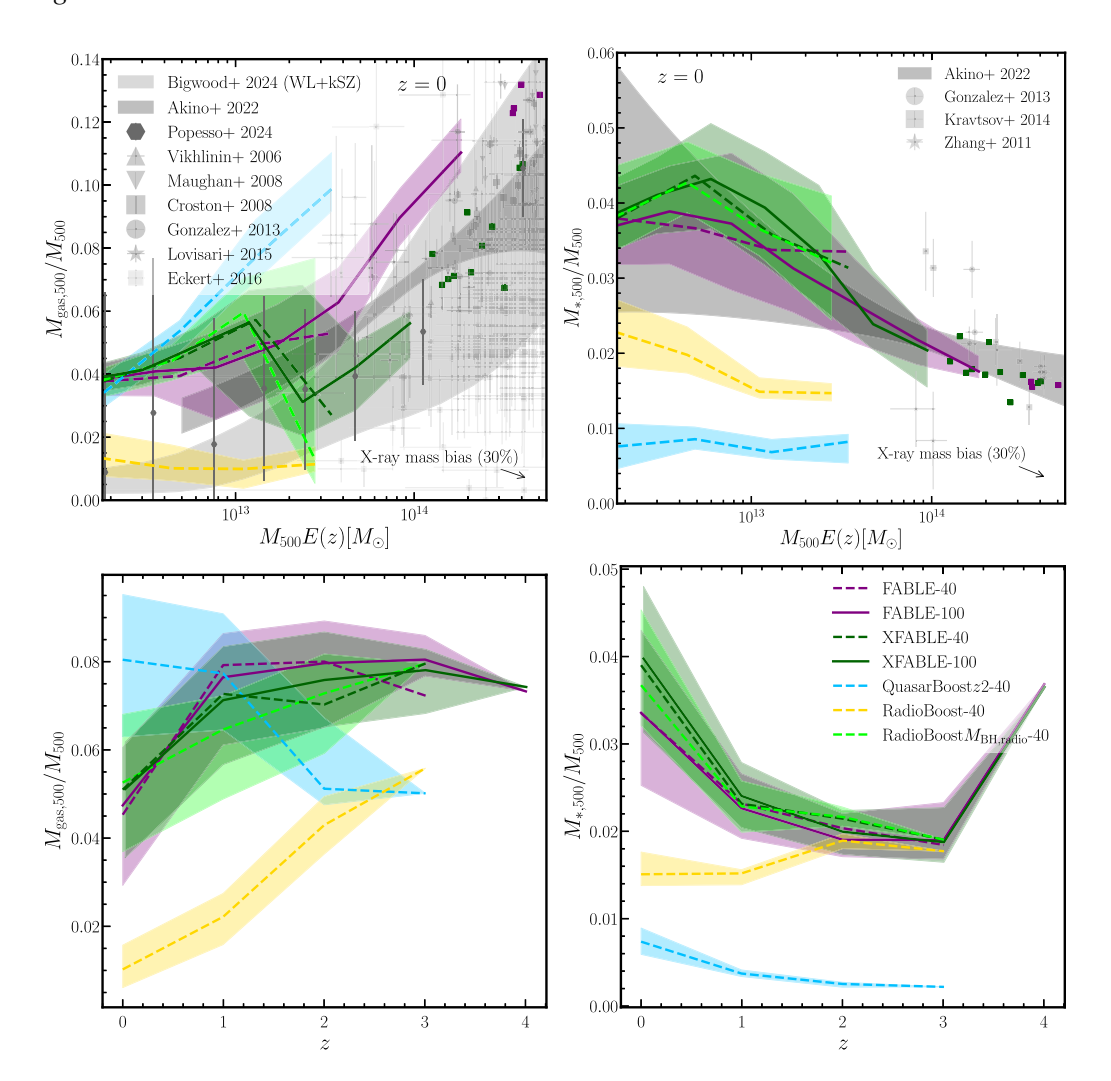


Figure 6. The hot gas mass and stellar mass fractions in each of our key simulation models, measured within r_{500} . The dashed lines denote (40 h^{-1} Mpc)³ boxes, and the solid lines show the (100 h^{-1} Mpc)³ FABLE and XFABLE boxes. For each box, the solid/dashed lines denote the median relation, and the shaded regions span the upper and lower quartiles of the distribution. We do not show the quartile regions of the FABLE-40 and XFABLE-40 boxes to avoid overcrowding the figure. For FABLE-100 and XFABLE-100, we plot the most massive systems that cannot be binned due to poor statistics as individual data points. We show the fiducial FABLE boxes (purple) and our key modified AGN feedback models: QuasarBoostz2-40 (light blue), RadioBoost-40 (yellow), RadioBoost $M_{BH,radio}$ -40 (light green), and XFABLE (dark green). *Upper left*: the hot gas mass fraction as a function of halo mass M_{500} at z = 0. The grey data points are the observation derived measurements of Popesso et al. (2024) (z < 0.2), Vikhlinin et al. (2006) (z < 0.25), Maughan et al. (2008) (0.1 < z < 1.3), Croston et al. (2008) (z < 0.2), Gonzalez et al. (2013) (z < 0.2), Lovisari et al. (2015) (z < 0.4), and Eckert et al. (2016) (0.05 < z < 1.1). The light grey shaded region shows the 1σ constraints derived from the joint weak lensing + kSZ analysis of Bigwood et al. (2024) and the dark grey shaded regions show the 1σ constraints of Gonzalez et al. (2013) (z < 0.2), Kravtsov, Vikhlinin & Meshcheryakov (2018) (z < 0.1), and Zhang et al. (2011) (z < 0.035). The grey shaded regions show the 1σ constraints of Onzalez et al. (2013) (z < 0.2), Kravtsov, Vikhlinin & Meshcheryakov (2018) (z < 0.1), and Zhang et al. (2011) (z < 0.035). The grey shaded regions show the 1σ constraints of Akino et al. (2022) (z < 1.1). An arrow is added to upper panels, indicating what would be the likely effect on X-ray-derived observations if one would correct for a hydrostatic mass bias of 30 per cent. *Lower panels:* the redshift

display a redshift evolution in the hot gas mass fraction in good agreement with fiducial FABLE. The RadioBoost-40 box however lies lower than FABLE at all redshifts shown, displaying gas fractions approximately half of those in FABLE already at z=2. This is due to the model's increased $D_{\rm bub}$ and $\chi_{\rm radio}$ parameters at all z, leading to the likely overejection of gas. As with the matter power spectrum suppression, the QuasarBoostz2-40 modification displays the opposite redshift trend to the other boxes. We find that the evolution is consistent with the previously discussed picture of overexpulsion of gas at z>2 and late-time re-accretion; the gas

mass fractions increase with time between 0 < z < 2, transitioning from lying below fiducial FABLE at z = 2 to lying above at z = 0.

To summarize, even by taking the considerable scatter in the observed hot gas fractions at face value, the RadioBoost-40 and QuasarBoostz2-40 models are largely disfavoured. The RadioBoost $M_{\rm BH,radio}$ -40 and XFABLE models can predict larger variations in hot gas fractions, and the new group-size data hint that radio-mode feedback could be even more effective that assumed in XFABLE for these low mass systems. Future X-ray and SZ data will be crucial to both constrain the required burstiness of

radio-mode feedback and how 'ejective' AGN feedback is likely to be as a function of cosmic time.

5.3.2 Stellar mass fractions

In the upper right panel of Fig. 6 we plot the stellar mass fraction in groups and clusters at z = 0, measured in the fiducial and modified FABLE boxes. We compute the total stellar mass within R_{500} without differentiating the contributions from the brightest central galaxy, satellite galaxies and the intracluster light, and refer the reader to Henden et al. (2020) where the stellar mass content of the individual components are studied in detail. We compare our results to the stellar mass-halo relation of Akino et al. (2022) derived from the XXL X-ray-selected sample, using the Hyper Suprime-Cam's photometry and weak-lensing mass measurements. We also plot X-ray measurements derived from a number of surveys: Gonzalez et al. (2013) (XMM–Newton), Kravtsov et al. (2018) (XMM–Newton, Chandra, and SDSS), and Zhang et al. (2011) (XMM-Newton, ROSAT, and SDSS), with the redshift ranges of the data listed in the figure caption. The cluster masses of Akino et al. (2022) are derived via weak lensing estimates, whereas the remaining sources use X-ray hydrostatic cluster masses. As in Fig. 1, we therefore add an arrow to Fig. 6 indicating the effect on observations of correcting for a hydrostatic mass bias of 30 per cent.

The fiducial FABLE-100 box displays a very good agreement with the observational data at z=0, consistent with the fit presented in Henden et al. (2018) for the FABLE-40 box. The RadioBoost $M_{\rm BH,radio}$ -40 and XFABLE modifications also lie in excellent agreement with fiducial FABLE and the available observations. As observed when discussing the GSMF (Section 5.2.1), the QuasarBoostz2-40 model significantly overquenches star formation, with less than ~ 1 per cent of the halo mass residing in stars at z=0. The stellar mass fraction in the RadioBoost-40 model also seems largely disfavoured by observational constraints at z=0, in line with our results for the GSMF.

The lower right panel of Fig. 6 shows the evolution in the stellar fractions for haloes with $M_{500} > 5 \times 10^{12} \,\mathrm{M}_{\odot}$ in each of the illustrative models. As with the hot gas mass fractions, we lack $z \ge 1$ observations of groups and clusters with masses overlapping those in FABLE, and therefore cannot at present directly benchmark the stellar fractions at higher redshifts, with our models providing useful predictions for future observations. FABLE, RadioBoost $M_{\rm BH,radio}$ -40, and XFABLE all display a comparable redshift evolution of the stellar mass fraction. RadioBoost-40 displays a stellar fraction in good agreement with FABLE at $z \ge 2$, however falls to a factor of \sim 2 lower by z=0 due to the prevalence of the extreme radio-mode at late cosmic times. QuasarBoostz2-40 exhibits stellar fractions that are a factor of \sim 4 lower than FABLE at all redshifts shown. In this model we note a marginal recovery in the stellar mass fractions at z < 2 as the quasar-mode feedback parameters return to the fiducial values, however this is insufficient to reach reasonable stellar fraction.

Fig. 7 shows the stellar mass fractions recomputed with M_{200} as the halo mass and calculating the stellar mass within twice the stellar half-mass radius, rather than within r_{500} . This facilitates comparison to the abundance matching models of, for example, Moster, Naab & White (2018), Behroozi et al. (2019), and Kravtsov et al. (2018), allowing us to benchmark our lowest mass groups. We find once again that fiducial FABLE, RadioBoost $M_{\rm BH,radio}$ -40, and XFABLE are all in good agreement with the abundance matching models for all group masses. At the massive end, our predicted stellar masses are

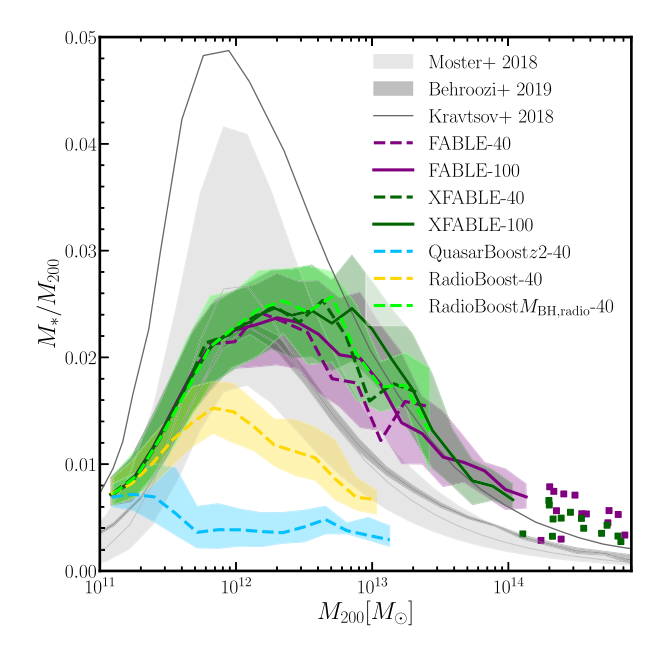


Figure 7. The stellar mass fractions in each of our key simulation boxes, recomputed with M_{200} as the halo mass and calculating the stellar mass within twice the stellar half-mass radius. The dashed lines denote $(40 \ h^{-1} \text{Mpc})^3$ boxes, and solid lines show the $(100 h^{-1}\text{Mpc})^3$ FABLE and XFABLE boxes. For each box, the solid/dashed lines denote the median relation, and the shaded regions span the upper and lower quartiles, calculated in bins of M_{500} . We do not show the quartile regions of the FABLE-40 and XFABLE-40 boxes to avoid overcrowding the figure. For FABLE-100 and XFABLE-100, we plot the most massive systems that cannot be binned due to poor statistics as individual data points. We show the fiducial FABLE boxes (purple) and our key modified AGN feedback models; QuasarBoostz2-40 (light blue), RadioBoost-40 (yellow), RadioBoostM_{BH,radio}-40 (light green) and XFABLE (dark green). We compare to the abundance matching models of Moster et al. (2018) (light grey), Behroozi et al. (2019) (medium grey) and Kravtsov et al. (2018) (dark grey). We show that the FABLE and XFABLE models are in equally good agreement with the abundance matching models.

somewhat too high with respect to the abundance matching models of Moster et al. (2018) and Behroozi et al. (2019), but agree quite well with the estimates from Kravtsov et al. (2018), indicating that the most massive galaxies in FABLE are reasonably realistic but perhaps not quite sufficiently quenched (Henden et al. 2020). As in the upper right panel of Fig. 6, the underestimation of the stellar mass in the QuasarBoostz2-40 and RadioBoost-40 models lead to their agreement with the observations at $M_{200} > 2 \times 10^{11} \, \mathrm{M}_{\odot}$ and $M_{200} > 5 \times 10^{11} \, \mathrm{M}_{\odot}$, respectively, being poor.

5.3.3 X-ray scaling relations

Thus far we have studied gas and stellar fraction of galaxy groups and clusters. Here, we extend our analysis of these objects by presenting scaling relations between global X-ray derived properties of groups and clusters for FABLE and our key modified feedback models. Comparing these to the wealth of observational data provides another benchmark that the AGN feedback model is able to produce a realistic cluster population, since the relations will be susceptible to independent model dependencies and systematics than cluster gas and stellar fraction measurements. We compare to a number of observational measurements from different surveys: Eckmiller, Hudson & Reiprich (2011) (Chandra), Mahdavi et al. (2013) (Chandra and XMM–Newton), Lovisari et al. (2015) (XMM–Newton, with

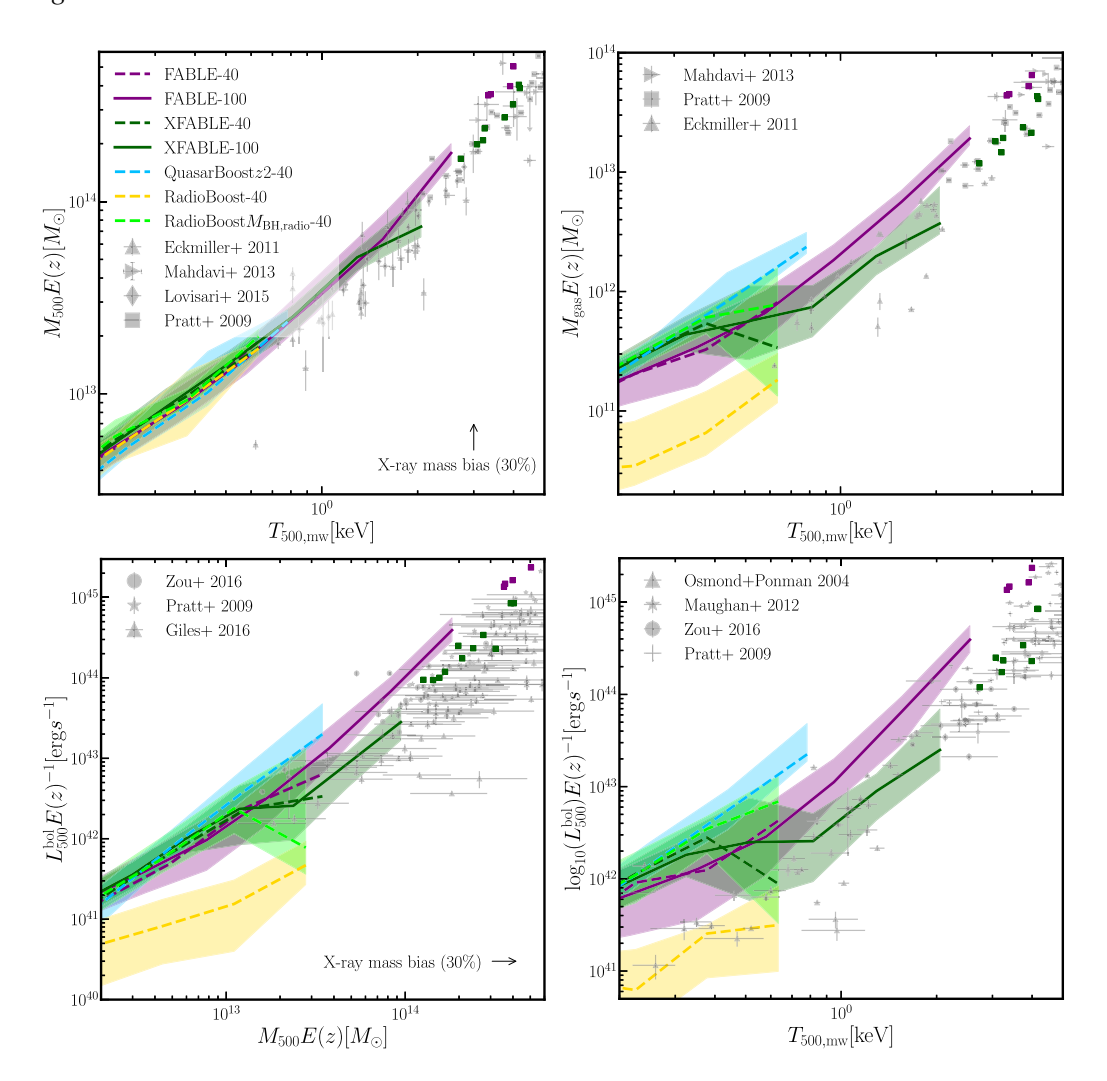


Figure 8. The z=0 scaling relations between halo mass M_{500} , hot gas mass $M_{\rm gas}$, X-ray hot ICM luminosity $L_{500}^{\rm bol}$, and the mass-weighted mean temperature $T_{500,\rm mw}$, measured in each of our key simulation models. All quantities are measured within r_{500} . The dashed lines denote $(40~h^{-1}{\rm Mpc})^3$ boxes, and solid lines show the $(100~h^{-1}{\rm Mpc})^3$ FABLE and XFABLE boxes. For each box, the solid/dashed lines denote the median relation, and the shaded regions span the upper and lower quartiles. We do not show the quartile regions of the FABLE-40 and XFABLE-40 boxes to avoid overcrowding the figure. For FABLE-100 and XFABLE-100, we plot the most massive systems that cannot be binned due to poor statistics as individual data points. We show the fiducial FABLE boxes (purple) and our key modified AGN feedback models; QuasarBoostz2-40 (light blue), RadioBoost-40 (yellow), RadioBoost $M_{\rm BH, radio}$ -40 (light green) and XFABLE (dark green). We plot as the grey data points the $M_{500}-T_{500,\rm mw}$ observational data of Eckmiller et al. (2011) (z<0.5), Mahdavi et al. (2013) (z<0.6), Lovisari et al. (2015) (z<0.4), Pratt et al. (2009) (z<0.2), the $M_{\rm gas}-T_{500}$ data of Mahdavi et al. (2013) (z<0.6), Pratt et al. (2009) (z<0.2), Eckmiller et al. (2011) (z<0.5), the $L_{500}^{\rm bol}-M_{500}$ data of Zou et al. (2016) (0.01 < z<0.05), Pratt et al. (2009) (z<0.2), Giles et al. (2016) (z<0.2), Giles et al. (2016) (z<0.2), and the $L_{500}^{\rm bol}-M_{500}$ data of Osmond & Ponman (2004), Maughan et al. (2012) (0.1 < z<0.05), Pratt et al. (2016) (0.01 < z<0.05) and Pratt et al. (2009) (z<0.2). We show that XFABLE displays an improved fit to the scaling relations compared to FABLE.

ROSAT-selected clusters), Pratt et al. (2009) (REXCESS XMM–Newton survey), Zou et al. (2016) (Chandra), Giles et al. (2016) (XXL survey, XMM–Newton), Osmond & Ponman (2004) (GEMS and ROSAT), and Maughan et al. (2012) (Chandra).

Fig. 8 plots the relations $M_{500}-T_{500,\rm mw}$ (upper left), $M_{\rm gas}-T_{500,\rm mw}$ (upper right), $L_{500}^{\rm bol}-M_{500}$ (lower left), and $L_{500}^{\rm bol}-T_{500}$ (lower right). We find that with the exception of the RadioBoost-40 and QuasarBoostz2-40 models, all the other AGN feedback models show scaling relations in very good agreement with fiducial FABLE, and with the observational data, with XFABLE displaying the best agreement for the most massive objects.

Consistent with Section 5.3.1, QuasarBoostz2-40 displays gas masses lying marginally higher than FABLE at all mean gas temperatures as well as increased ICM X-ray luminosities due to too high gas fractions at variance with observational data. The RadioBoost-

40 model appears at variance with observations for most scaling relations examined, but the overlap with data is limited.

Finally, we note that at low $T_{500,\mathrm{mw}}$ all our simulation models overpredict X-ray bolometric luminosities, apart from the RadioBoost-40 model (see bottom right panel). This finding is interesting, as it likely indicates that our luminosities and hence gas fractions ¹² may be too high in the lowest mass systems in agreement with leatest X-ray measurements from eROSITA (Popesso et al. 2024), as well as the indications from the kSZ effect (Bigwood et al. 2024; Hadzhiyska et al. 2024) (see Fig. 6).

¹²This is unlikely an effect of unrealistic ICM temperatures, see detailed reasoning in Henden et al. (2018).

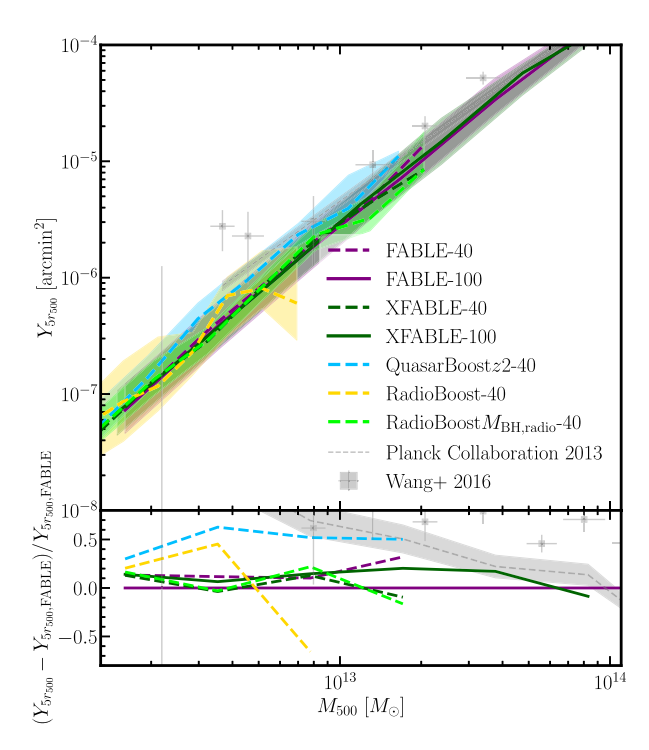


Figure 9. The tSZ-halo mass relation, $Y_{5r_{500}} - M_{500}$, at z = 0 measured in each of our key simulation models. We compute $Y_{5r_{500}}$ by measuring the Compton Y parameter within a spherical aperture of $5r_{500}$ (as motivated in Section 3.3.6) and rescaling to a fixed angular diameter distance of 500 Mpc. The dashed lines denote $(40 \ h^{-1} \mathrm{Mpc})^3$ boxes, and the solid lines show the $(100 \ h^{-1}{\rm Mpc})^3$ FABLE and XFABLE boxes. For each box, the solid/dashed lines denote the median relation, and the shaded regions span the upper and lower quartiles. We do not show the quartile regions of the FABLE-40 and XFABLE-40 boxes to avoid overcrowding the figure. We show the fiducial FABLE boxes (purple) and our key modified AGN feedback models; QuasarBoostz2-40 (light blue), RadioBoost-40 (yellow), RadioBoostM_{BH,radio}-40 (light green) and XFABLE (dark green). We compare to the observationally derived best-fitting scaling relation of Planck Collaboration XI (2013) (grey dashed line and shaded region) and the recalibration of the Planck Collaboration XI (2013) data by Wang et al. (2016) (grey square data points). We do not extrapolate the Planck Collaboration XI (2013) relation to lower halo-masses than the last well constrained datapoint. To examine the differences between the predicted $Y_{5r_{500}}-M_{500}$ in each box with greater clarity, the lower sub-panel shows the fractional difference between the median $Y_{5r_{500}}-M_{500}$ relation as measured in the fiducial FABLE box and the remaining models, $(Y_{5r_{500}} - Y_{5r_{500},FABLE})/Y_{5r_{500},FABLE}$. We similarly re-scale the observational data in the lower panel. We demonstrate that modified AGN feedback boxes produce a reasonable fit to the data, albeit being somewhat low, with some variation in the predictions between models.

5.3.4 The tSZ $Y_{5r_{500}} - M_{500}$ relation

X-ray measurements of the ICM typically probe the most massive, and thus X-ray luminous, clusters in the Universe (but see recent work by Popesso et al. 2024). SZ measurements provide a unique and complementary window into feedback as a result of its sensitivity to higher redshift systems, as well as groups and low mass clusters, which are believed to be more affected than massive clusters by AGN-driven gas ejection due to their shallower gravitational potential wells. Comparison of observed tSZ scaling relations with simulation predictions therefore provide insights into feedback's impact on a different cluster population to that studied with X-rays, with measurements prone to an independent set of systematics. Fig. 9 shows the $Y_{5r_{500}} - M_{500}$ relation calculated in FABLE and each of the key

AGN feedback simulation models, with the lower subplot displaying the residual $Y_{5r_{500}}$ with respect to fiducial FABLE. We compare the simulated results to the Planck Collaboration XI (2013) $Y_{r_{500}} - M_{500}$ measurements (with halo masses estimated using the stellar masshalo mass relation derived from a galaxy formation simulation), as well as the re-analysis of Wang et al. (2016) with weak-lensing calibrated masses. As a result, neither data set is susceptible to X-ray hydrostatic mass bias. As discussed in Section 3.3.6, we multiply $Y_{r_{500}}$ in both observational data sets by a factor of 1.796 in order to obtain $Y_{5r_{500}}$ and avoid the modelling assumptions used in the *Planck* analyses.

We find that each of the modified feedback boxes, with the exception of QuasarBoostz2-40 and RadioBoost-40, show little deviation to FABLE in the slope and amplitude of the $Y_{5r_{500}} - M_{500}$ relation. Since $Y_{5r_{500}}$ provides a measure of a group's thermal energy, this indicates that the RadioBoost $M_{\rm BH,radio}$ -40 and XFABLE feedback models likely do not overheat the systems, as was previously reflected in the GSMF (Section 5.2.1), which analogously showed that there was sufficient cool gas in these models for realistic star formation. The QuasarBoostz2-40 model displays a higher amplitude of the $Y_{5r_{500}} - M_{500}$ relation, which is consistent with higher gas fraction due to low-redshift gas re-accretion in this model. It also shows an improved agreement over FABLE, when compared to the observed relation of Planck Collaboration XI (2013) and Wang et al. (2016), but for wrong reasons given that higher amplitude is driven by a too large amount of ICM gas.

The RadioBoost-40 model measures a low $Y_{5r_{500}}$ for group-scale haloes. This indicates that the feedback has expelled sufficient gas beyond r_{500} to significantly reduce the thermal energy of groups. This, as previously hinted at in the X-ray scaling relations (Section 5.3.3), informs us that the low GSMF at z=0 discussed in Section 5.2.1 results from the feedback model leading to galaxies being gaspoor, rather than effective star formation being prevented through overheating. We verify this picture in Section 3.3.7, where we gain insight into the local thermodynamic processes acting within groups through the radial profiles.

5.3.5 The X-ray $Y_{X,500} - M_{500}$ relation

The final global cluster property we explore in Fig. 10 is the X-ray analogue of the Compton $Y_{r_{500}}$ parameter, $Y_{X,500}$. We compute the $Y_{X,500}-M_{500}$ relation for FABLE and each of our modified feedback boxes, and compare to the measurements of Maughan et al. (2008) (*Chandra*), Arnaud, Pointecouteau & Pratt (2007) (*XMM–Newton*) and Eckmiller et al. (2011) (*Chandra*).

Alike $Y_{5r_{500}}$, $Y_{X,500}$ is similarly sensitive to the thermal energy of groups and clusters within r_{500} (Kravtsov et al. 2006). We therefore find broadly the same relationship between the $Y_{X,500}-M_{500}$ relation from our key simulation models as detailed in Section 5.3.4; i.e. the relation measured in FABLE and each of the modified feedback models display similar slopes, however the amplitude of the RadioBoost-40 model lies low. For groups of mass $M_{500}\sim 10^{13}\,{\rm M}_{\odot}$, $Y_{X,500}$ is approximately half the value in the RadioBoost-40 box compared to FABLE and can be ruled out by the observations. Both the FABLE-100 and XFABLE-100 models remain in agreement with the observations, with the two models showing little deviation in their predicted relation.

5.4 Thermodynamic profiles of the ICM

In this section, we compute spherically averaged radial profiles of the ICM in order to validate the local thermodynamical properties

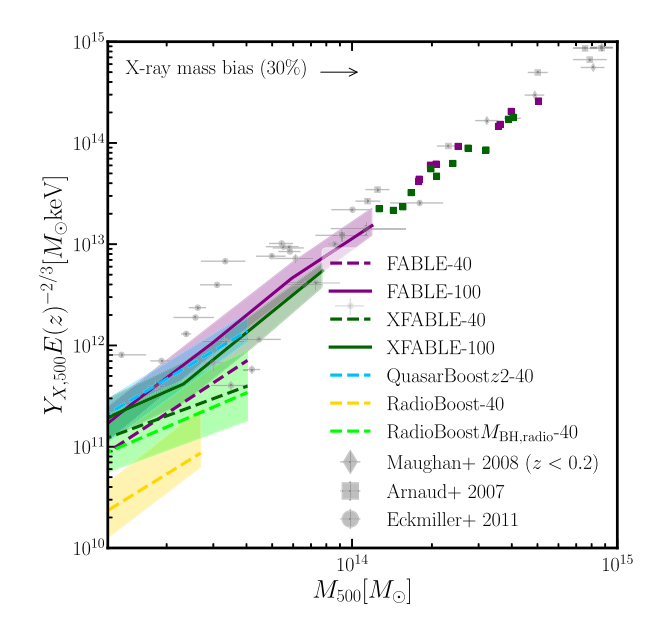


Figure 10. The $Y_{X,500} - M_{500}$ measured in each of our key simulation boxes. Here, $Y_{X,500}$ is the X-ray proxy of the tSZ Compton Y_{500} parameter, measured within a spherical aperture of radius r_{500} according to equation (11). The dashed lines denote $(40 h^{-1} \text{Mpc})^3$ boxes, and the solid lines show the $(100 h^{-1} \text{Mpc})^3$ FABLE and XFABLE boxes. For each box, the solid/dashed lines denote the median relation, and the shaded regions span the upper and lower quartiles. We do not show the quartile regions of the FABLE-40 and XFABLE-40 boxes to avoid overcrowding the figure. For FABLE-100 and XFABLE-100, we plot the most massive systems that cannot be binned due to poor statistics as individual data points. We show the fiducial FABLE boxes (purple) and our key modified AGN feedback models; QuasarBoostz2-40 (light blue), RadioBoost-40 (yellow), RadioBoostM_{BH,radio}-40 (light green), and XFABLE (dark green). We compare our simulation measured relations to the observational measurements of Maughan et al. (2008) (plotting only the clusters at z < 0.2), Arnaud et al. (2007) (z < 0.2) and Eckmiller et al. (2011) (z < 0.05), shown as the grey data points. We show that alike FABLE, XFABLE also lies in good agreement with the observational data.

of our simulated groups and clusters. Fig. 11 shows the mean profile weighted by halo mass for haloes within a given halo mass range matched to observations, as well as the 1σ region spanned by the sample of simulated profiles. We measure profiles of the electron number density (n_e) , the dimensionless temperature (T/T_{500}) , the dimensionless pressure (P/P_{500}) and the dimensionless entropy (K/K_{500}) in FABLE and each of our modified feedback boxes. We compare to the measured profiles of Sun et al. (2009) (*Chandra*), and the electron density profiles of Pratt et al. (2022) (*XMM–Newton* REXCESS sample).

We have followed common practice in normalizing the dimension-less profiles T/T_{500} , P/P_{500} and K/K_{500} under the assumption that a self-similar model holds, in order to remove the mass-dependent trends and facilitate comparison between haloes of different masses. This procedure however does not remove the potential mass bias that may exist between simulations and the observations we compare to, and typically such a bias has not been mitigated for in previous comparisons. Since the halo mass is related to the characteristic temperature by $T_{500} \propto M_{500}^{2/3}$, correcting for a typical 30 per cent hydrostatic mass bias in the Sun et al. (2009) halo mass estimates would shift the masses to larger values and therefore the observed dimensionless radial temperature profiles to lower values (and similar for the pressure and entropy profiles, since $P_{500} \propto M_{500}^{2/3}$ and $K_{500} \propto M_{500}^{2/3}$). Furthermore as $r_{500} \propto M_{500}^{1/3}$, correcting for a

hydrostatic mass bias would shift all observed profiles plotted in Fig. 11 to smaller radii. As discussed in Henden et al. (2018), another important consideration is the sample selection. If groups or clusters are selected within a given halo mass range to compare with observations, the effective mass range may differ between simulations and the X-ray data due to the mass bias. Finally, since the observed groups and clusters are X-ray selected and thus biased toward the most X-ray luminous systems, even when halo masses are matched, the observed profiles may show additional scatter. For example, the electron density profiles may span a broader range and extend to lower densities. Each of these considerations should be kept in mind when comparing simulations and observations, and we refer the reader to Henden et al. (2018) for a more detailed discussion.

The FABLE-100 box remains consistent with the FABLE-40 box, which was verified in Henden et al. (2018) to produce very good agreement with the measured thermodynamic profiles of Sun et al. (2009). As anticipated from our previous analysis, and recalling that the RadioBoost-40 model allows for a larger fraction of black holes to be in the radio-mode, as well as injecting AGN-driven bubbles at a greater distance from the galaxy centre, it is not surprising that this model leads to an ICM with high-entropy outskirts, low-pressure inner regions, and in general reduced electron density, rendering the model incompatible with observations. The QuasarBoostz2-40 model predicts somewhat too high mean gas densities and too low mean temperatures for the intermediate range of spatial scales, 0.2 < $r/r_{500} < 0.5$. The RadioBoost $M_{\rm BH, radio}$ -40 modification, which we recall implements a boosted radio-mode in only the heaviest SMBHs, has thus far remained largely consistent against the galaxy, group and cluster observations we have tested it against. The thermodynamic profiles however indicate that this model leads to too strong shock heating of the ICM. The mean density and pressure profiles are systematically lower than observational profiles at all radii, and the entropy and temperature profiles around $r/r_{500} \sim 0.5 - 0.6$ display characteristic signatures of ICM overheating by too powerful AGN feedback, motivating the addition of a pressure-limit in the XFABLE model.

The XFABLE model produces thermodynamic profiles that remain in good agreement with the observational measurements. This highlights the importance of modelling AGN-driven bubble feedback as a 'gentle' heating processes. Nevertheless, XFABLE predicts somewhat lower densities within groups and clusters, as well as lower gas pressures and higher gas entropy outskirts, which hint that this model is likely too effective at heating the ICM. Matching the observed ICM profiles from small groups to most massive clusters, as well as reproducing the cool core versus non-cool core population remains one of the very important benchmarks for theoretical models of AGN feedback.

6 DISCUSSION AND CONCLUSIONS

Cosmological analyses using non-linear scales crucially rely on accurate theoretical predictions of the baryonic physics impact on the matter power spectrum. However, state-of-the-art cosmological galaxy formation simulations, such as FLAMINGO (Schaye et al. 2023), MillenniumTNG (Pakmor et al. 2023), SIMBA (Davé et al. 2019), BAHAMAS (McCarthy et al. 2017), FABLE (Henden et al. 2018), Horizon-AGN (Dubois et al. 2014), and Magneticum (Steinborn et al. 2015), currently do not provide a consensus view on this fundamental issue, as too large uncertainties persist in our understanding of modus operandi of stellar and AGN feedback processes. This astrophysical model uncertainty limits cosmological precision of weak lensing analyses (e.g. Amon et al. 2022; Dark

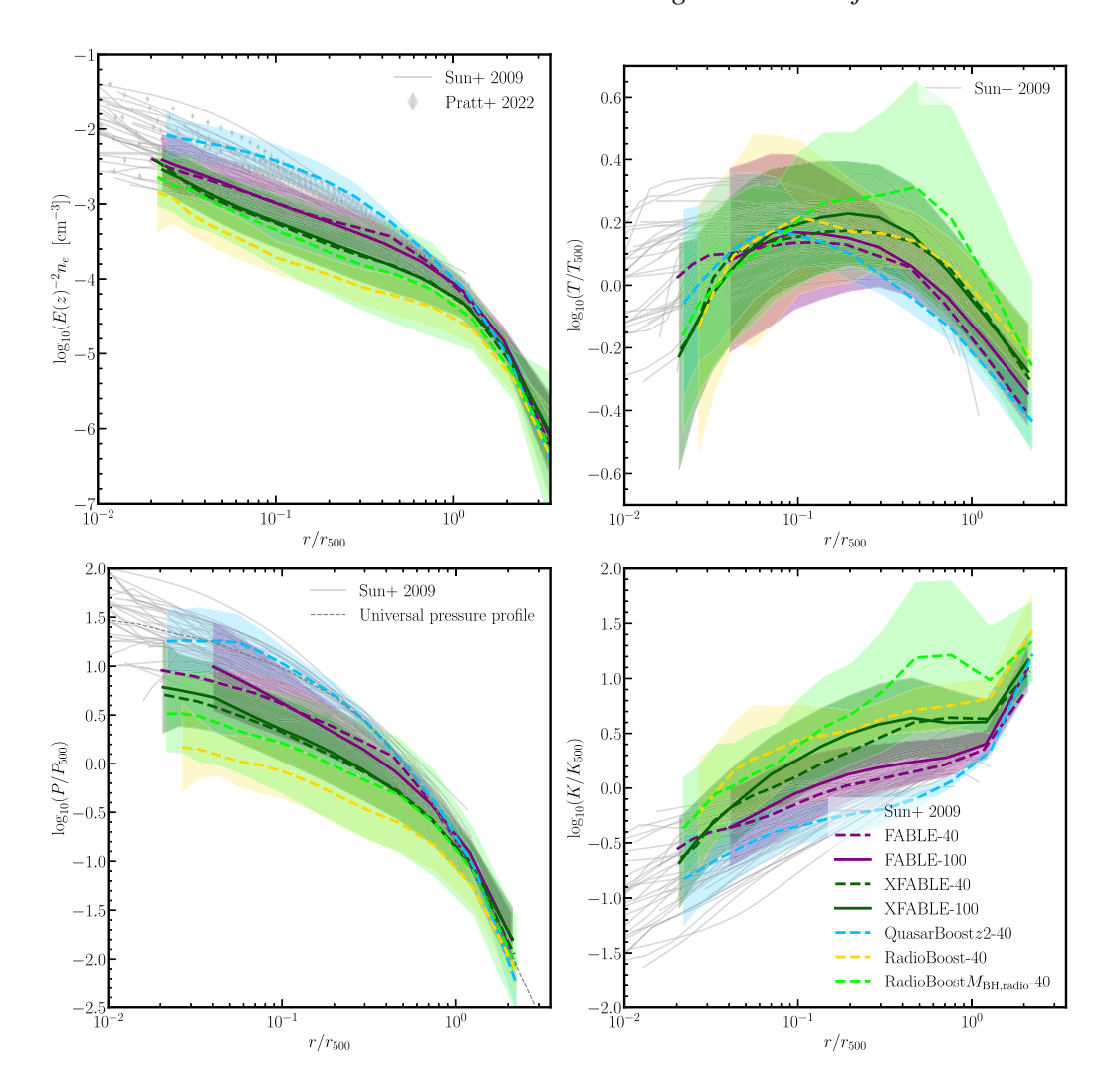


Figure 11. Thermodynamic radial profiles of the hot ICM measured in each of our key simulation boxes at z = 0. In each panel, we compare to the Sun et al. (2009) observationally derived ICM profiles (shown as the grey lines) and therefore compute profiles for simulated haloes with masses lying within the range spanned by Sun et al. (2009) sample, $1.48 \times 10^{13} < M_{500}$ [M_☉] < 1.49×10^{14} . For the electron density profiles, we also compare to a sample of Pratt et al. (2022) profiles which include several heavier haloes and therefore compute profiles for simulated haloes with masses $1.48 \times 10^{13} < M_{500}$ [M_☉] < 1.89×10^{14} . For each box, the solid/dashed lines denote the mean profile weighted by halo mass and the shaded regions show the 1σ region spanned by the simulated profile sample. We do not show the 1σ region of the FABLE-40 and XFABLE-40 boxes to avoid overcrowding the figure. The dashed lines denote (40 h^{-1} Mpc)³ boxes, and the solid lines show the (100 h^{-1} Mpc)³ FABLE and XFABLE boxes. We show the fiducial FABLE boxes (purple) and our key modified AGN feedback models; QuasarBoostz2-40 (light blue), RadioBoost-40 (yellow), RadioBoost $M_{\rm BH,radio}$ -40 (light green) and XFABLE (dark green). *Upper left:* Electron number density profiles of the ICM. *Upper right:* Dimensionless temperature profile of the ICM, normalized by the characteristic temperature T_{500} (equation 14). *Lower left:* Dimensionless pressure profiles of the ICM, normalized by the characteristic entropy K_{500} (equation 15). We compare to the measurements of Sun et al. (2009) (0.012 < z < 0.12) and Pratt et al. (2022) (0.056 < z < 0.108) when available.

Energy Survey and Kilo-Degree Survey Collaboration 2023), and it is possible that underestimating feedback effects can bias current constraints or mask the ability to test for signatures of models beyond ΛCDM (Amon & Efstathiou 2022; Preston et al. 2023). In the upcoming era of the Rubin Observatory Legacy Survey of Space and Time, the Euclid mission, and the *Nancy Grace Roman Space Telescope*, pinning down the amplitude and extent of the suppression of the matter power spectrum due to 'baryonic feedback' is critical.

Recent studies indicate that 'baryonic feedback' may be more extreme than state-of-the-art hydrodynamical simulations (Preston et al. 2023; Bigwood et al. 2024; McCarthy et al. 2024). Furthermore, recent eROSITA measurements that probe systems down to low-mass groups point towards lower gas fractions (Popesso et al. 2024).

Motivated by these findings, we have explored a range of AGN feedback models built around the FABLE project (Henden et al. 2018; Henden et al. 2019, 2020) to understand the plausibility of stronger AGN feedback models.

We have performed a large simulation suite that systematically explores AGN feedback models that act differently either as a function of cosmic time, host halo properties, and/or spatial location where feedback energy is effectively coupled with the surrounding medium. Within this suite we found a viable AGN feedback model, XFABLE, that causes strong matter power spectrum suppression on large scales ($k \lesssim 1 \ h \ \mathrm{Mpc^{-1}}$). To achieve this, AGN radio-mode feedback needs to (i) act in larger population of black holes with respect to the FABLE model (i.e. below the Eddington accretion rate

ratio of \approx 0.1); (ii) (at least) operate in halo hosts that have a well-developed 'hot atmosphere' ($M_{500} \approx 10^{13} \, \mathrm{M}_{\odot}$); and (iii) have jet lobes thermalizing at relatively large cluster-centric distances ($\approx 100 \, h^{-1} \mathrm{kpc}$). Our main findings from our simulation suite are as follows:

- (i) To produce sufficiently large matter power spectrum suppression consistent with the latest observational constraints (e.g. Bigwood et al. 2024), AGN feedback needs to redistribute large amounts of gas towards outskirts of groups and clusters. This process cannot operate only at early cosmic times, as gas re-accretion on to the growing cluster's potential wells needs to be prevented at low redshifts. This process also needs to act across a range of halo masses up to the largest galaxy clusters probed by our simulations $(M_{500} \sim 5 \times 10^{14} \, \mathrm{M}_{\odot})$ to cause sufficient matter power spectrum suppression at low k values, $k \lesssim 1 \, h \, \mathrm{Mpc}^{-1}$ (in agreement with findings from e.g. van Loon & van Daalen 2024; Martin-Alvarez et al. 2024).
- (ii) While AGN feedback needs to push sufficient amounts of gas to large cluster-centric distances, strong AGN feedback, which removes the *central* gas reservoir, is clearly disfavoured. Such modelling choice easily overquenches central galaxies, with the observed GSMF at different redshifts providing stringent constraints on the amount of central cold gas that is needed to build realistic galaxy stellar masses.
- (iii) Several of our key simulation models produce a reasonable cosmological population of SMBHs, with black hole-host galaxy scaling relations and redshift evolution of QLF in agreement with observations. Comparisons to these observables do not allow us to constrain AGN feedback models, which produce markedly different matter power spectrum suppressions.
- (iv) Importantly, we found a novel empirical AGN feedback model, XFABLE, that is able to produce large matter power spectrum suppression at low k-values while maintaining a very good agreement with GSMF, gas fractions in groups and clusters, and all key galaxy cluster X-ray and tSZ scaling relations. This indicates that there may exist a physically plausible galaxy formation model within the Λ CDM Universe, which is consistent with all current observational constraints from this diverse range of data sets, without the need to invoke alternative cosmological models.
- (v) Interestingly, both recent joint weak lensing + kSZ (Bigwood et al. 2024) and X-ray constraints (Popesso et al. 2024) indicate that the gas fraction in a few times 10^{12} – 10^{13} M $_{\odot}$ systems may be even lower than in the XFABLE model, but we emphasize that to produce matter power suppression on large scales ($k \lesssim 1 \, h \, \text{Mpc}^{-1}$), accurately modelling AGN feedback effects in more massive haloes is the key.
- (vi) Unsurprisingly, radial profiles of key thermodynamical properties of the ICM provide crucial constraints on the nature and modus operandi of AGN feedback, facilitating to differentiate between the models that eject too much gas versus the models that overheat the gas at large radii. XFABLE retains good agreement with ICM radial profiles, but our detailed comparison clearly points towards the need to more self-consistently model AGN bubble inflation via jets and to account for the relativistic population within the jet lobes.

The XFABLE model is deliberately constructed to impact gas at larger cluster-centric distances and allows for a larger population of SMBHs to act in radio-mode. However, if such an AGN feedback model is physically viable, the fundamental question remains for how it operates in detail. Tantalizingly, recent LOFAR observations have revealed AGN-driven radio jets spanning ~ 7 Mpc from the host galaxy with stellar mass of $\sim 5.5-6.7\times 10^{11}\,\mathrm{M}_{\odot}$ (Oei et al. 2024), which would directly heat the IGM. LOFAR's LoTSS DR2

survey has recently revealed more than 10 000 of such giant radio galaxies (Mostert et al. 2024), with ILoTSS and SKA providing constrains on this rapidly rising population in the near future. These observational findings suggest that for a sufficiently large fraction of systems, radio lobes may well be inflated at large distances from the central galaxy proving a direct heating source at large-scales. None the less, future observations constraining this population and detailed numerical simulations of magnetized relativistic jets in full cosmological simulations will be needed to understand jet energetics and the likely thermalization of the surrounding medium (Ehlert et al. 2018; Bourne, Sijacki & Puchwein 2019; Bourne & Sijacki 2021).

It is important to stress that a large range of AGN models explored in this work, which lead to markedly different matter power spectrum suppressions, still rely on the underlying FABLE-like baryonic physics modelling. Specifically, we have not explored any variations to star formation and associated stellar feedback models, and we have not explored alternative black hole accretion prescriptions or different heating channels, such as cosmic-ray-driven or radiationpressure-driven outflows, for example. This highlights that the parameter space of baryonic physics modelling is much more vast than that explored here (or within most state-of-the-art large cosmological simulations) and that there may be even more degeneracies within models of these complex processes and the signatures they leave on the matter power spectrum. The range in the matter power spectrum suppression spanned by the various simulations (left panel of Fig. 1) may therefore significantly widen, before it is better constrained by observations. We stress that in cosmological analyses, it is critical that feedback mitigation strategies are flexible enough to capture the extent of the feedback modelling uncertainties, considering the potential degeneracies in the power suppression.

The future observational landscape to unravel how 'baryonic feedback' operates is promising. eROSITA is already transforming our knowledge of galaxy clusters and groups, probing into lowmass regime. Gas fraction measurements and detections of spatially resolved ICM properties of group-sized objects both locally and at high redshifts, via X-rays with eROSITA, and the Athena X-ray observatory in future, will provide crucial constraints on the nature of AGN feedback as a function of cosmic time. X-ray detections of hot gas in filaments and of the warm-hot intergalactic medium will provide complementary constraints on the baryon cycle and gas redistribution from groups and clusters. Upcoming weak lensing surveys will also allow us to reconstruct the non-linear matter power spectrum, allowing us to distinguish between different models of 'baryonic feedback' (Preston et al. 2024). Moreover, thermal and kinetic SZ observations with ACT and shortly with the Simons Observatory, both via stacking and characterization of individual systems, will independently constrain galaxy group and cluster gas properties, probing both lower mass systems and feedback effects at large cluster-centric distances. Furthermore, constrains on the stellar mass assembly of brightest cluster galaxies that large galaxy surveys such as LSST and Euclid will elucidate the role of 'ejective' AGN feedback as well as constrain stellar feedback channels in these system. Radio facilities such as CHIME (CHIME/FRB Collaboration 2021) are also rapidly expanding the catalogue of detected fast radio bursts (FRBs), which enable direct measurements of the free electron column density out to large cosmological distances, thereby tracing the baryon distribution (see e.g. Medlock et al. 2025). This work will pave the way for constraining feedback processes across cosmic time using upcoming FRB catalogues, including the tens of thousands expected to be detected by CHORD (Vanderlinde et al. 2019). Finally, LOFAR has uncovered an unprecedented population of giant radio galaxies, and with ILoTSS and SKA on the horizon we will soon get

D'Souza R., Vegetti S., Kauffmann G., 2015, MNRAS, 454, 4027

Croston J. H. et al., 2008, A&A, 487, 431

a much better insight into the crucial issue of AGN jet energy transfer into the surrounding medium. Together with the rapid advancement of galaxy formation simulations, which are now starting to tackle complex physics of radiation effects on the fly, cosmic-ray-driven feedback, and black hole physics through realistic accretion discs and magnetized relativistic jets, our ability to constrain baryonic physics for precision cosmology is within reach.

ACKNOWLEDGEMENTS

We thank George Efstathiou for useful discussions throughout this work, and feedback on the manuscript. We also thank Joop Schaye for comments on the draft. LB, MAB, and DS acknowledge support from the Science and Technology Facilities Council (STFC). VI acknowledges the support of the Kavli Foundation and PD51-INFN INDARK grant. MAB acknowledges support from a UKRI Stephen Hawking Fellowship (EP/X04257X/1). The simulations were performed on the DiRAC Darwin Supercomputer hosted by the University of Cambridge High Performance Computing Service (http://www.hpc.cam.ac.uk/), provided by Dell Inc. using Strategic Research Infrastructure Funding from the Higher Education Funding Council for England and funding from the Science and Technology Facilities Council. Simulations were also performed using the COSMA Data Centric system at Durham University, operated by the Institute for Computational Cosmology on behalf of the STFC DiRAC HPC Facility. This equipment was funded by a BIS National E-infrastructure capital grant ST/K00042X/1, STFC capital grant ST/K00087X/1, DiRAC Operations grant ST/K003267/1, and Durham University.

DATA AVAILABILITY

The data used in this work may be shared on reasonable request to the authors.

```
REFERENCES
Akino D. et al., 2022, PASJ, 74, 175
Amon A., Efstathiou G., 2022, MNRAS, 516, 5355
Amon A. et al., 2022, Phys. Rev. D, 105, 023514
Arnaud M., Pointecouteau E., Pratt G. W., 2007, A&A, 474, L37
Arnaud M., Pratt G. W., Piffaretti R., Böhringer H., Croston J. H., Pointe-
   couteau E., 2010, A&A, 517, A92
Baldry I. K. et al., 2012, MNRAS, 421, 621
Begelman M. C., Cioffi D. F., 1989, ApJ, 345, L21
Behroozi P., Wechsler R. H., Hearin A. P., Conroy C., 2019, MNRAS, 488,
Bernardi M., Meert A., Sheth R. K., Vikram V., Huertas-Company M., Mei
   S., Shankar F., 2013, MNRAS, 436, 697
Bernardi M. et al., 2018, MNRAS, 475, 757
Bigwood L. et al., 2024, MNRAS, 534, 655
Booth C. M., Schaye J., 2009, MNRAS, 398, 53
Borgani S., Governato F., Wadsley J., Menci N., Tozzi P., Lake G., Quinn T.,
   Stadel J., 2001, ApJ, 559, L71
Bourne M. A., Sijacki D., 2021, MNRAS, 506, 488
Bourne M. A., Yang H.-Y. K., 2023, Galaxies, 11, 73
Bourne M. A., Zubovas K., Nayakshin S., 2015, MNRAS, 453, 1829
Bourne M. A., Sijacki D., Puchwein E., 2019, MNRAS, 490, 343
Chabrier G., 2003, PASP, 115, 763
CHIME/FRB Collaboration, 2021, ApJS, 257, 59
```

Churazov E., Sazonov S., Sunyaev R., Forman W., Jones C., Böhringer H.,

Chisari N. E. et al., 2019, Open J. Astrophys. 2, 4

Crichton D. et al., 2016, MNRAS, 458, 1478

2005, MNRAS, 363, L91

```
Dark Energy Survey and Kilo-Degree Survey Collaboration, 2023, Open J.
   Astrophys., 6, 36
Davé R., Anglés-Alcázar D., Narayanan D., Li Q., Rafieferantsoa M. H.,
   Appleby S., 2019, MNRAS, 486, 2827
Davis M., Efstathiou G., Frenk C. S., White S. D. M., 1985, ApJ, 292, 371
DESI Collaboration, 2025a, J. Cosmol. Astropart. Phys., 2025, 021
DESI Collaboration, 2025b, J. Cosmol. Astropart. Phys., 2025, 028
Di Matteo T., Springel V., Hernquist L., 2005, Nature, 433, 604
Dolag K., Borgani S., Murante G., Springel V., 2009, MNRAS, 399, 497
Driver S. P. et al., 2022, MNRAS, 513, 439
Dubois Y. et al., 2014, MNRAS, 444, 1453
Dutta Chowdhury D., Chatterjee S., 2017, ApJ, 839, 34
Eckert D. et al., 2016, A&A, 592, A12
Eckmiller H. J., Hudson D. S., Reiprich T. H., 2011, A&A, 535, A105
Efstathiou G., McCarthy F., 2025. MNRAS, 540, 1055
Ehlert K., Weinberger R., Pfrommer C., Pakmor R., Springel V., 2018,
   MNRAS, 481, 2878
Fabian A. C., 2012, ARA&A, 50, 455
Fabjan D., Borgani S., Tornatore L., Saro A., Murante G., Dolag K., 2010,
   MNRAS, 401, 1670
Faucher-Giguère C.-A., Lidz A., Zaldarriaga M., Hernquist L., 2009, ApJ,
   703, 1416
Ferreira T., Alonso D., Garcia-Garcia C., Chisari N. E., 2024, Phys. Rev.
   Lett., 133, 051001
Gebhardt M. et al., 2024, MNRAS, 529, 4896
Genel S. et al., 2014, MNRAS, 445, 175
Giles P. A. et al., 2016, A&A, 592, A3
Gonzalez A. H., Sivanandam S., Zabludoff A. I., Zaritsky D., 2013, ApJ, 778,
Greene J. E., Strader J., Ho L. C., 2020, ARA&A, 58, 257
Habouzit M. et al., 2022, MNRAS, 509, 3015
Hadzhiyska B. et al., 2024, preprint (arXiv:2407.07152)
Hardcastle M. J., Croston J. H., 2020, New Astron. Rev., 88, 101539
Hardcastle M. J., Krause M. G. H., 2013, MNRAS, 430, 174
Harrison C. M., Alexander D. M., Mullaney J. R., Swinbank A. M., 2014,
   MNRAS, 441, 3306
Heinz S., Reynolds C. S., Begelman M. C., 1998, ApJ, 501, 126
Henden N. A., Puchwein E., Shen S., Sijacki D., 2018, MNRAS, 479, 5385
Henden N. A., Puchwein E., Sijacki D., 2019, MNRAS, 489, 2439
Henden N. A., Puchwein E., Sijacki D., 2020, MNRAS, 498, 2114
Hlavacek-Larrondo J., Li Y., Churazov E., 2022, in Bambi C., Sangangelo
   A., eds, Handbook of X-ray and Gamma-ray Astrophysics. p. 5
Ilbert O. et al., 2013, A&A, 556, A55
Katz N., Weinberg D. H., Hernquist L., 1996, ApJS, 105, 19
Kormendy J., Ho L. C., 2013, ARA&A, 51, 511
Koudmani S., Sijacki D., Smith M. C., 2022, MNRAS, 516, 2112
Kravtsov A. V., Vikhlinin A., Nagai D., 2006, ApJ, 650, 128
Kravtsov A. V., Vikhlinin A. A., Meshcheryakov A. V., 2018, Astron. Lett.,
Kroupa P., 2001, MNRAS, 322, 231
La Posta A., Alonso D., Chisari N. E., Ferreira T., García-García C., 2025,
   Phys. Rev. D, 112, 043525
Lau E. T. et al., 2025, ApJ, 984, 190
Le Brun A. M. C., McCarthy I. G., Schaye J., Ponman T. J., 2014, MNRAS,
   441, 1270
Li C., White S. D. M., 2009, MNRAS, 398, 2177
Lovisari L., Reiprich T. H., Schellenberger G., 2015, A&A, 573, A118
Madau P., Dickinson M., 2014, ARA&A, 52, 415
Madhavacheril M. S. et al., 2024, ApJ, 962, 113
Mahdavi A., Hoekstra H., Babul A., Bildfell C., Jeltema T., Henry J. P., 2013,
   ApJ, 767, 116
Marinacci F., Pakmor R., Springel V., 2014, MNRAS, 437, 1750
Martin-Alvarez S., Iršič V., Koudmani S., Bourne M., Bigwood L., Sijacki
   D., 2024, MNRAS, 539, 1738
Maughan B. J., Jones C., Forman W., Van Speybroeck L., 2008, ApJS, 174,
   117
```

Maughan B. J., Giles P. A., Randall S. W., Jones C., Forman W. R., 2012, MNRAS, 421, 1583

McCarthy I. G. et al., 2010, MNRAS, 406, 822

McCarthy I. G., Schaye J., Bird S., Le Brun A. M. C., 2017, MNRAS, 465, 2936

McCarthy I. G. et al., 2024, MNRAS, 540, 143

Medlock I., Nagai D., Anglés-Alcázar D., Gebhardt M., 2025, ApJ, 983, 46

Moster B. P., Somerville R. S., Maulbetsch C., van den Bosch F. C., Macciò A. V., Naab T., Oser L., 2010, ApJ, 710, 903

Moster B. P., Naab T., White S. D. M., 2018, MNRAS, 477, 1822

Mostert R. I. J. et al., 2024, A&A, 691, A185

Mullaney J. R., Alexander D. M., Fine S., Goulding A. D., Harrison C. M., Hickox R. C., 2013, MNRAS, 433, 622

Muzzin A. et al., 2013, ApJ, 777, 18

Oei M. S. S. L. et al., 2024, Nature, 633, 537

Osmond J. P. F., Ponman T. J., 2004, MNRAS, 350, 1511

Pakmor R., Springel V., Bauer A., Mocz P., Munoz D. J., Ohlmann S. T., Schaal K., Zhu C., 2016, MNRAS, 455, 1134

Pakmor R. et al., 2023, MNRAS, 524, 2539

Pan Z. et al., 2023, Phys. Rev. D, 108, 122005

Pandey S. et al., 2023, MNRAS, 525, 1779

Planck Collaboration VI, 2020, A&A, 641, A6

Planck Collaboration XI, 2013, A&A, 557, A52

Popesso P. et al., 2024, A&A, preprint (arXiv:2411.16555)

Power C., Navarro J. F., Jenkins A., Frenk C. S., White S. D. M., Springel V., Stadel J., Quinn T., 2003, MNRAS, 338, 14

Pratt G. W., Croston J. H., Arnaud M., Böhringer H., 2009, A&A, 498, 361

Pratt G. W., Arnaud M., Biviano A., Eckert D., Ettori S., Nagai D., Okabe N., Reiprich T. H., 2019, Space Sci. Rev., 215, 25

Pratt G. W., Arnaud M., Maughan B. J., Melin J. B., 2022, A&A, 665, A24

Preston C., Amon A., Efstathiou G., 2023, MNRAS, 525, 5554

Preston C., Amon A., Efstathiou G., 2024, MNRAS, 533, 621

Reines A. E., Volonteri M., 2015, ApJ, 813, 82

Ruan J. J., McQuinn M., Anderson S. F., 2015, ApJ, 802, 135

Rybicki G. B., Lightman A. P., 1985, Radiative Processes in Astrophysics. Wiley, New York, https://cds.cern.ch/record/847173

Salcido J., McCarthy I. G., Kwan J., Upadhye A., Font A. S., 2023, MNRAS, 523, 2247

Salpeter E. E., 1955, ApJ, 121, 161

Santini P. et al., 2012, A&A, 538, A33

Schaller M., Schaye J., Kugel R., Broxterman J. C., van Daalen M. P., 2025, MNRAS, 539, 1337

Schaye J. et al., 2015, MNRAS, 446, 521

Schaye J. et al., 2023, MNRAS, 526, 4978

Scheuer P. A. G., 1974, MNRAS, 166, 513

Schneider A., Teyssier R., Stadel J., Chisari N. E., Le Brun A. M. C., Amara A., Refregier A., 2019, J. Cosmol. Astropart. Phys., 2019, 020

Semboloni E., Hoekstra H., Schaye J., van Daalen M. P., McCarthy I. G., 2011, MNRAS, 417, 2020

Shen X., Hopkins P. F., Faucher-Giguère C.-A., Alexander D. M., Richards G. T., Ross N. P., Hickox R. C., 2020, MNRAS, 495, 3252

Sijacki D., Springel V., Di Matteo T., Hernquist L., 2007, MNRAS, 380, 877

Sijacki D., Vogelsberger M., Genel S., Springel V., Torrey P., Snyder G. F., Nelson D., Hernquist L., 2015, MNRAS, 452, 575

Springel V., 2010, MNRAS, 401, 791

Springel V., Hernquist L., 2003, MNRAS, 339, 289

Springel V., White S. D. M., Tormen G., Kauffmann G., 2001, MNRAS, 328, 726

Springel V., Di Matteo T., Hernquist L., 2005, MNRAS, 361, 776

Springel V. et al., 2018, MNRAS, 475, 676

Steinborn L. K., Dolag K., Hirschmann M., Prieto M. A., Remus R.-S., 2015, MNRAS, 448, 1504 Sun M., Voit G. M., Donahue M., Jones C., Forman W., Vikhlinin A., 2009, ApJ, 693, 1142

Torrey P., Vogelsberger M., Genel S., Sijacki D., Springel V., Hernquist L., 2014, MNRAS, 438, 1985

van Daalen M. P., Schaye J., Booth C. M., Dalla Vecchia C., 2011, MNRAS, 415, 3649

van Daalen M. P., McCarthy I. G., Schaye J., 2020, MNRAS, 491, 2424

van Loon M. L., van Daalen M. P., 2024, MNRAS, 528, 4623

Vanderlinde K. et al., 2019, Canadian Long Range Plan for Astronomy and Astrophysics White Papers. p. 28

Vikhlinin A., Kravtsov A., Forman W., Jones C., Markevitch M., Murray S. S., Van Speybroeck L., 2006, ApJ, 640, 691

Villaescusa-Navarro F., 2018, Astrophysics Source Code Library, record ascl:1811.008

Vogelsberger M., Genel S., Sijacki D., Torrey P., Springel V., Hernquist L., 2013, MNRAS, 436, 3031

Vogelsberger M., Marinacci F., Torrey P., Puchwein E., 2020, Nat. Rev. Phys., 2, 42

Voit G. M., Balogh M. L., Bower R. G., Lacey C. G., Bryan G. L., 2003, ApJ, 503, 272

Wang W., White S. D. M., Mandelbaum R., Henriques B., Anderson M. E., Han J., 2016, MNRAS, 456, 2301

Weinberger R. et al., 2018, MNRAS, 479, 4056

Wiersma R. P. C., Schaye J., Smith B. D., 2009a, MNRAS, 393, 99

Wiersma R. P. C., Schaye J., Theuns T., Dalla Vecchia C., Tornatore L., 2009b, MNRAS, 399, 574

Zhang Y. et al., 2024a, A&A, 690, A267

Zhang Y. et al., 2024b, A&A, 690, A268

Zhang Y. Y., Laganá T. F., Pierini D., Puchwein E., Schneider P., Reiprich T. H., 2011, A&A, 535, A78

Zou S., Maughan B. J., Giles P. A., Vikhlinin A., Pacaud F., Burenin R., Hornstrup A., 2016, MNRAS, 463, 820

APPENDIX A: THE IMPACT OF COSMIC VARIANCE

In this appendix, we investigate the effect of cosmic variance on the matter power spectrum suppression due to 'baryonic feedback'. We run five $(40 h^{-1}\text{Mpc})^3$ simulations with the fiducial FABLE model, testing five different values of the random seed that determines the initial Gaussian density field (with 'Seed 0' being the random seed utilized for all boxes described in the main text). Fig. A1 demonstrates that the choice of random seed has a nonnegligable impact on the matter spectrum suppression at z = 0. At $k = 5 h \,\mathrm{Mpc^{-1}}$ we see variations in the predicted suppression of ~ 5 per cent. The maximum suppression varies by a similar amount, with the location of the maxima shifting marginally between boxes, lying in the range $k \sim 7-10 \, h \, {\rm Mpc}^{-1}$. The difference in predictions between variations of the initial Gaussian density field results from the different numbers of the high-mass haloes realized by z = 0, exasperated by the limited box size. Since AGNs exhibiting the most extreme feedback live in these rare overdense environments (Daalen et al. 2020), the suppression due to 'baryonic feedback' effects is affected by cosmic variance due to the different numbers of powerful AGNs realized. Our results using the larger $(100 \ h^{-1}\text{Mpc})^3$ boxes should be relatively robust to these effects, but even larger box sizes are desirable to fully test the convergence of the models to the box size (see e.g. Daalen et al. 2020; Pakmor et al. 2023; Schaller et al. 2025).

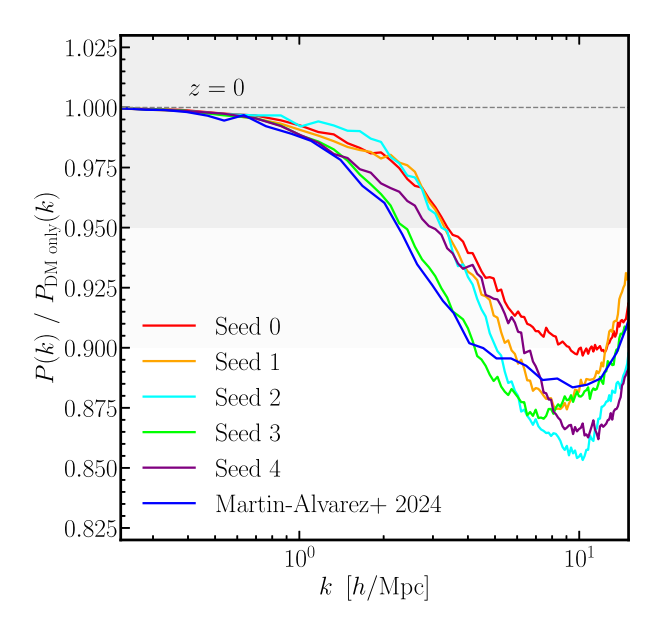


Figure A1. The impact of cosmic variance on the z=0 matter power spectrum due to baryonic effects, $P(k)/P_{\rm DM}$, measured in $(40~h^{-1}{\rm Mpc})^3$ FABLE boxes. The coloured lines show the measured $P(k)/P_{\rm DM}$ in $(40~h^{-1}{\rm Mpc})^3$ simulations ran with different values of random seed that determines the initial Gaussian density field. Seed 0 is the FABLE-40 box, ran with the random seed utilized for all boxes described in the main text. We plot the suppression measured in the FABLE $(40~h^{-1}{\rm Mpc})^3$ box presented in Henden et al. (2018) and Martin-Alvarez et al. (2024), which was also ran with a different random seed to that utilized in this work.

APPENDIX B: FULL SIMULATION SUITE

Table B1 lists the key parameter choices for the full suite of FABLE-like modified AGN feedback simulation boxes ran in this work.

Table B1. The key AGN feedback parameters utilized in the full suite of FABLE-like $(40 \ h^{-1} \text{Mpc})^3$ simulations ran for this work. Parameters follow the definitions in Table 1, adding $M_{\rm BH,radio}$ as the black hole mass limit above which radio-mode feedback is allowed to occur (introduced in Section 4.3) and $E_{\rm bub}/E_{\rm ICM}$ as the limit on the energy content of radio-mode bubbles (introduced in Section 4.4). A parameter that varies with redshift, z, as a step function is represented in the format z < 2:30, z > 2:100, where in this example 30 is the value of the parameter for z < 2 and 100 is its value for z > 2. A linear evolution in a parameter is represented in the format $z = 0:30 \rightarrow z = 4:500$, where in this example the parameter is fixed to 500 at z > 4, and decreases linearly to 30 by z = 0.

Simulation name	Xradio	α	ϵ_f	Δt [Myr]	$\epsilon_{ m m}$	$D_{\rm bub} \\ [{\rm kpc}h^{-1}]$	$R_{\rm bub}$ [kpc h^{-1}]	$M_{\rm BH,radio}$ [10 ¹⁰ M $_{\odot}$ h^{-1}]	$E_{ m bub}/E_{ m ICM}$
Fiducial box settings FABLE	0.01	100	0.1	25	0.8	30	50	-	_
z-dependent quasar-mode QuasarBoostz2	0.01	$z < 2:100^a,$ $z > 2:10^4$		25	0.8	30	50	-	-
$\underline{z ext{-dependent }\epsilon_m ext{ in radio-mode}}$ -	0.01	100	0.1	25	z < 2:0.8, z > 2:8	30	50	-	-
$\frac{z\text{-dependent }D_{\text{bub}}\text{ in radio-mode}}{-}$	0.01^{b}	100^{b}	0.1^{b}	25	0.8	z < 2:30, z > 2:100	50 ^b	-	-
RadioBoost	0.1 ^c	100	0.1	25	0.8^{c}	$z = 0:30 \rightarrow$ $z = 4:500^{c}$	50	-	_
$\frac{\textit{M}_{BH}\text{-threshold for radio-mode}}{\text{RadioBoost}\textit{M}_{BH, radio}}$	0.1	100	0.1	25	0.8	100^d	50	0.06^{d}	_
$\frac{\text{further } E_{\text{bub}}/E_{\text{ICM}} \text{ limiter}}{\text{XFABLE}}$	0.1^{e}	100	0.1	25	0.8	100^{e}	50	0.06^{f}	20 ^g

Notes. ^a Keeping other parameters the same, we also tested combinations of (i) fixing $\alpha = 100$ at all z, (ii) setting α to 1000 for z > 2, (iii) fixing $\epsilon_f = 0.1$ at all z, and (iv) setting ϵ_f to 1 for z > 2.

This paper has been typeset from a TEX/LATEX file prepared by the author.

^bKeeping other parameters the same, we also tested boxes with (i) $\chi_{\text{radio}} = 0.1$, $\alpha = 1000$, $\epsilon_f = 1$ and (ii) $\chi_{\text{radio}} = 0.1$, $R_{\text{bub}} = 20$.

^cKeeping other parameters the same, we tested combinations of (i) $\chi_{\rm radio} = 0.01, 0.05$, (ii) a linear evolution of ϵ_m as $z = 0: 0.1 \rightarrow z = 4: 0.8$, (iii) setting $D_{\rm bub}$ to 300 for z > 4, (iv) setting $D_{\rm bub}$ to 100 at z = 0, and (v) keeping $D_{\rm bub}$ fixed for 0 < z < 1.

^dKeeping other parameters the same, we also explored $D_{\text{bub}} = 30, 50, 150, 200 \text{ and } M_{\text{BH,radio}} = 0.01.$

^eKeeping other parameters the same, we tested changing χ_{radio} to 0.02, and D_{bub} to 200, 500.

^f We also explored $M_{\rm BH,radio} = 0.02$.

^gKeeping other parameters the same, we also tested $E_{\text{bub}}/E_{\text{ICM}} = 2, 4, 6, 50, 100, 200, 500, 800.$